A&A 598, A122 (2017)
DOI: 10.1051/0004-6361/201629301


Astronomy & Astrophysics

# The WISSH quasars project

## I. Powerful ionised outflows in hyper-luminous quasars

M. Bischetti[1,2], E. Piconcelli[1], G. Vietri[1,3], A. Bongiorno[1], F. Fiore[1], E. Sani[4], A. Marconi[5,6], F. Duras[7,1], L. Zappacosta[1], M. Brusa[8,9], A. Comastri[9], G. Cresci[6], C. Feruglio[10,1], E. Giallongo[1], F. La Franca[7], V. Mainieri[11], F. Mannucci[6], S. Martocchia[1], F. Ricci[7], R. Schneider[3,1], V. Testa[1], and C. Vignali[8,9]

[1] INAF–Osservatorio Astronomico di Roma, via Frascati 33, 00078 Monte Porzio Catone (Roma), Italy
e-mail: manuela.bischetti@oa-roma.inaf.it
[2] Università degli Studi di Roma "Tor Vergata", via Orazio Raimondo 18, 00173 Roma, Italy
[3] Università degli Studi di Roma "La Sapienza", Piazzale Aldo Moro 5, 00185 Roma, Italy
[4] European Southern Observatory (ESO), Alonso de Cordova 3107, Cassilla 19001, Vitacura, Santiago 19, Chile
[5] Dipartimento di Fisica e Astronomia, Università di Firenze, via G. Sansone 1, 50019 Sesto Fiorentino (Firenze), Italy
[6] INAF–Osservatorio Astrofisico di Arcetri, Largo E. Fermi 5, 50125 Firenze, Italy
[7] Dipartimento di Matematica e Fisica, Università degli Studi Roma Tre, via della Vasca Navale 84, 00146 Roma, Italy
[8] Dipartimento di Fisica e Astronomia, Università di Bologna, viale Berti Pichat 6/2, 40127 Bologna, Italy
[9] INAF–Osservatorio Astronomico di Bologna, via Ranzani 1, 40127 Bologna, Italy
[10] INAF–Osservatorio Astronomico di Trieste, via G.B. Tiepolo 11, 34143 Trieste, Italy
[11] European Southern Observatory, Karl-Schwarzschild-str. 2, 85748 Garching bei München, Germany

Received 13 July 2016 / Accepted 9 December 2016

**ABSTRACT**

Models and observations suggest that both the power and effects of AGN feedback should be maximised in hyper-luminous ($L_{\rm Bol} > 10^{47}$ erg s$^{-1}$) quasars, i.e. objects at the brightest end of the AGN luminosity function. In this paper, we present the first results of a multiwavelength observing programme, focusing on a sample of WISE/SDSS selected hyper-luminous (WISSH) broad-line quasars at $z \approx 1.5$–5. The WISSH quasars project has been designed to reveal the most energetic AGN-driven outflows, estimate their occurrence at the peak of quasar activity, and extend the study of correlations between outflows and nuclear properties up to poorly investigated, extreme AGN luminosities, i.e. $L_{\rm Bol} \sim 10^{47}$–$10^{48}$ erg s$^{-1}$. We present near-infrared, long-slit LBT/LUCI1 spectroscopy of five WISSH quasars at $z \approx 2.3$–3.5, showing prominent [OIII] emission lines with broad (FWHM ∼1200–2200 km s$^{-1}$) and skewed profiles. The luminosities of these broad [OIII] wings are the highest measured so far, with $L^{\rm broad}_{[OIII]} \gtrsim 5 \times 10^{44}$ erg s$^{-1}$, and reveal the presence of powerful ionised outflows with associated mass outflow rates $\dot{M} \gtrsim 1700\ M_\odot$ yr$^{-1}$ and kinetic powers $\dot{E}_{\rm kin} \gtrsim 10^{45}$ erg s$^{-1}$. Although these estimates are affected by large uncertainties because of the use of [OIII] as a tracer of ionised outflows and the very basic outflow model adopted here, these results suggest that in our hyper-luminous targets the AGN is highly efficient at pushing large amounts of ionised gas outwards. Furthermore, the mechanical outflow luminosities measured for WISSH quasars correspond to higher percentages (∼1–3%) of $L_{\rm Bol}$ than those derived for AGN with lower $L_{\rm Bol}$. Our targets host very massive ($M_{\rm BH} \gtrsim 2 \times 10^9\ M_\odot$) black holes that are still accreting at a high rate (i.e. a factor of ∼0.4–3 of the Eddington limit). These findings clearly demonstrate that WISSH quasars offer the opportunity to probe the extreme end of both luminosity and supermassive black holes (SMBH) mass functions and revealing powerful ionised outflows that are able to affect the evolution of their host galaxies.

**Key words.** galaxies: active – galaxies: nuclei – quasars: emission lines – quasars: general – quasars: supermassive black holes – techniques: imaging spectroscopy

## 1. Introduction

The energy output produced as a result of accretion on supermassive black holes (SMBHs) can be larger than the gravitational binding energy in their host galaxies, and it is therefore expected to have a substantial role in their evolution (Silk & Rees 1998; Wyithe & Loeb 2003; King & Pounds 2015). Models of galaxy formation indeed invoke active galactic nuclei (AGN)-driven feedback to suppress the excessive growth of massive galaxies and drive their evolution from gas-rich starburst galaxies to red and dead ellipticals (Hopkins et al. 2008; Somerville et al. 2008). There is a general consensus regarding AGN-driven outflows as the most efficient feedback mechanism to deplete and/or heat the interstellar medium (ISM) and, possibly, quench star formation (Menci et al. 2008; Zubovas & King 2012; Costa et al. 2014).

Recently, a rapidly flourishing literature on AGN winds has been growing with the discovery of multiple observational examples in all (i.e. molecular and atomic, neutral and ionised) gas phases (e.g. Feruglio et al. 2015; Maiolino et al. 2012; Fabian 2012; Harrison et al. 2012; Spoon et al. 2013; Rupke & Veilleux 2015; Brusa et al. 2015; Morganti et al. 2016), with kinetic powers clearly indicating that these winds must originate from nuclear activity consistent with the expectations of AGN feedback and galaxy co-evolution models (see Fiore et al. 2016, and references therein). In particular, the observation of emission lines, typically [OIII]$\lambda$4959, 5007 Å, with broad, skewed, blue- and redshifted profiles has been the main tool to prove that ionised

gas winds are a nearly ubiquitous feature in AGN (Zhang et al. 2011; Mullaney et al. 2013; Shen & Ho 2014). Thanks to spatially resolved spectroscopy, it has been possible to reveal galaxy-wide, kpc-scale [OIII] outflows in dozens of AGN (e.g. Nesvadba et al. 2006, 2008; Harrison et al. 2012, 2014; Liu et al. 2013; Carniani et al. 2015; Perna et al. 2015b) and infer their mass outflow rate and kinetic power, with measured $\dot{M}$ and $\dot{E}_{\rm kin}$ up to ~600–700 $M_{\odot}\,{\rm yr}^{-1}$ and ~$0.01 \times L_{\rm Bol}$, respectively. Furthermore, in some cases, the outflowing [OIII] emission has been found to be spatially anti-correlated with narrow H$\alpha$ emission, which traces star formation in the host galaxy (Cano-Díaz et al. 2012; Cresci et al. 2015; Carniani et al. 2016). These results are considered among the most compelling pieces of evidence of negative feedback from AGN reported so far.

Remarkably, both models and observations indicate that the AGN efficiency in driving energetic winds and the momentum fluxes of galaxy-scale outflows increase with AGN luminosity (e.g. Menci et al. 2008; Faucher-Giguère & Quataert 2012; Cicone et al. 2014; Feruglio et al. 2015; Hopkins et al. 2016). Understanding the coupling between the nuclear energy output and the ISM in the host galaxy is thus particularly relevant in the context of hyper-luminous AGN (i.e. quasars with $L_{\rm Bol} > 10^{47}$ erg s$^{-1}$), lying at the bright end of the AGN luminosity function. A systematic, multiwavelength investigation of nuclear, outflow, star formation, and ISM properties of hyper-luminous quasars is therefore clearly needed to understand the impact of their huge radiative output on the host galaxy evolution. More specifically, the role of AGN luminosity in accelerating winds and providing an efficient feedback, and the occurrence of powerful outflows in hyper-luminous systems at the peak epoch of quasar and star formation activity (i.e. at $z \sim 2$–3), are key aspects that deserve a detailed study in order to be answered. To address these open issues, we designed a multi-band (from millimetre wavelengths up to hard X-rays) investigation of a large sample of WISE/SDSS selected hyper-luminous (WISSH) quasars.

In this paper, which is the first of a series that will focus on WISSH quasars, we present observations and physical parameters of AGN-driven ionised outflows traced by broad [OIII] emission lines, which have been detected in the rest-frame optical spectra of five quasars at $z \sim 2.3$–3.5. In Sect. 2, we describe the WISSH quasars sample and the main goals of our ongoing project. Details about LBT observations and data reduction are presented in Sect. 3. In Sect. 4, we measure the extinction and outline the models used in our spectral analysis. In Sect. 5, we present the results of the spectral fitting, i.e. the best-fit models and emission lines parameters, and the analysis of the "off-nuclear" spectra performed to detect the possible presence of extended [OIII] emitting gas. H$\beta$-based SMBH masses and Eddington ratios are presented in Sect. 5.3. In Sect. 6, we discuss the properties of the broad [OIII] emission derived from our observations in the context of luminous quasars, and we compare the mass rate and kinetic power of the outflows of WISSH quasars with those found for lower luminosity AGN samples. We summarise our findings in Sect. 7.

Throughout this paper, we assume $H_0 = 70$ km s$^{-1}$ Mpc$^{-1}$, $\Omega_{\Lambda} = 0.73$ and $\Omega_{\rm M} = 0.27$.

## 2. The WISSH quasars project

We are following up the properties of a quasars sample compiled by Weedman et al. (2012), consisting of 100 Type 1 AGN at $z \gtrsim 1.5$ with a flux density $S_{22\,\mu{\rm m}} > 3$ mJy, selected by cross-correlating the WISE all-sky source catalogue (Wright et al. 2010) with the SDSS DR7 catalogue. Our sample of WISSH quasars has been obtained by removing lensed objects and those with a contaminated WISE photometry from the original list of Weedman et al. (2012) and consists of 86 quasars at $z \sim 1.8$–4.6. As stressed by Weedman et al. (2012), WISSH quasars represent the most luminous AGN known in the Universe with bolometric luminosities $L_{\rm Bol} > 10^{47}$ erg s$^{-1}$. By selecting Type 1 SDSS quasars, we include sources affected by low extinction and for which it is possible to reliably measure the SMBH mass via broad emission linewidths. The vast majority of the existing works focused on AGN-driven feedback has been concentrated on AGN samples with redshifts and luminosities smaller than those of WISSH sources (e.g. Harrison et al. 2012, 2016; Rupke & Veilleux 2013; Wylezalek & Zakamska 2016). The WISSH survey is specifically designed to investigate systematically the outflows properties in $L_{\rm Bol} > 10^{47}$ erg s$^{-1}$ quasars at cosmic noon, i.e. $z \sim 2$–3, when SMBH accretion and star formation have reached their maximum; the survey also complements previous literature on observational evidence for AGN feedback.

The main goal of our WISSH project is to probe the properties of nuclear and star formation activity in these hyper-luminous quasars and the effects of AGN feedback on their host galaxies via spectroscopic, imaging, and photometric observations. An extensive, multi-band, observing programme is indeed currently ongoing, based on ALMA, SINFONI, X-shooter, TNG, *XMM-Newton*, and *Chandra* data (the project also benefits from publicly available *Herschel*, WISE, 2MASS, and SDSS data) to obtain a panchromatic, less-biased view of these extreme sources. Such a large amount of data indeed enables us to properly build the spectral energy distribution (SED), investigate the different ISM phases, and constrain the SMBH mass and accretion rate of WISSH quasars. Furthermore, WISSH quasars allow us to improve the study of correlations between outflows and nuclear properties by bringing the explorable range up to $L_{\rm Bol} \sim 10^{47-48}$ erg s$^{-1}$.

## 3. LBT observations and data reduction

In this paper, we present the first results of the WISSH quasars project. We were awarded observing time with the Near-Infrared Spectrograph and Imager (LUCI1) at the 8.4 m Large Binocular Telescope (LBT), located on Mount Graham (Arizona), to perform moderate resolution ($R \sim 4000$) near-IR spectroscopy of 18 WISSH quasars. The aim of these observations is to reveal possible broad- and blueshifted [OIII] components that are indicative of ionised outflows. These objects belong to a subsample of WISSH quasars selected by removing sources with (i) $z > 3.6$ and $1.6 < z < 2$ (i.e. for which LUCI1 does not cover the [OIII] spectral region); (ii) no available 2MASS $JHK$ magnitudes; and (iii) a redshift for which telluric lines contaminate the [OIII] emission line or the LBT/LUCI1 bandwidth does not simultaneously cover both [OIII] and H$\beta$ emission lines. Eight targets were observed during Cycle 2014, while the remaining targets belong to Cycle 2015.

Here we focus on the five quasars (namely J0745+4734, J0900+4215, J1201+1206, J1326−0005, and J1549+1245) that exhibit prominent, broad [OIII] emission. The complete analysis and results for the whole LUCI1 WISSH quasars sample, consisting of 18 objects, will be reported in a forthcoming paper (Vietri et al.). Table 1 lists coordinates, SDSS 10th data release (DR10) redshift and optical photometric data (Ahn et al. 2014), and 2MASS near-IR photometric data (Skrutskie et al. 2006) for the five WISSH quasars analysed here.

**Table 1.** Properties of the five analysed WISSH quasars.

| SDSS | RA | Dec | $z_{SDSS}$ | $u$ | $g$ | $r$ | $i$ | $z$ | $J$ | $H$ | $K_s$ |
|---|---|---|---|---|---|---|---|---|---|---|---|
| (1) | (2) | (3) | (4) | (5) | (6) | (7) | (8) | (9) | (10) | (11) | (12) |
| J0745+4734 | 07:45:21.78 | +47:34:36.1 | 3.214 | 19.56 | 16.63 | 16.35 | 16.29 | 16.19 | 15.08 | 14.61 | 13.95 |
| J0900+4215 | 09:00:33.50 | +42:15:47.0 | 3.295 | 22.97 | 17.11 | 16.74 | 16.69 | 16.58 | 15.37 | 14.68 | 14.00 |
| J1201+1206 | 12:01:47.90 | +12:06:30.3 | 3.484 | 20.77 | 18.31 | 17.41 | 17.31 | 17.18 | 15.87 | 15.25 | 14.61 |
| J1326−0005 | 13:26:54.95 | −00:05:30.1 | 3.307 | 22.83 | 20.90 | 20.54 | 20.02 | 19.28 | 17.39 | 16.75 | 15.31 |
| J1549+1245 | 15:49:38.71 | +12:45:09.1 | 2.386 | 20.23 | 18.67 | 17.84 | 17.38 | 16.90 | 15.86 | 14.56 | 13.52 |

**Notes.** Columns give the following information: (1) SDSS ID; (2–3) celestial coordinates; (4) redshift from the SDSS DR10 catalogue; (5–9) photometric data from the SDSS DR10 catalogue; (10–12) photometric data from the 2MASS catalogue.

**Table 2.** Journal of the LBT/LUCI1 observations.

| SDSS | Grating | $R$ | $t_{exp}$ | Seeing | Obs date | Std. star |
|---|---|---|---|---|---|---|
| (1) | (2) | (3) | (4) | (5) | (6) | (7) |
| J0745+4734 | 150 $K_s$ | 4150 | 600 | 0.90 | Jan. 10th 2015 | HIP 35787 |
| J0900+4215 | 150 $K_s$ | 4150 | 800 | 1.0 | Jan. 10th 2015 | HIP 35787 |
| J1201+1206 | 150 $K_s$ | 4150 | 1500 | 0.72 | Apr. 20th 2014 | HIP 64231 |
| J1326−0005 | 150 $K_s$ | 4150 | 2500 | 0.79 | Apr. 20th 2014 | HIP 64231 |
| J1549+1245 | 210 $zJHK$ | 7838 | 1500 | 0.66 | Apr. 20th 2014 | HIP 68868 |

**Notes.** Columns give the following information: (1) SDSS ID; (2) grating; (3) resolution; (4) exposure time (in units of s); (5) average seeing (in units of arcsec); (6) observation date; and (7) standard star.

The LUCI1 observations of our targets were carried out in long-slit mode (1 arcsec slit at position angle PA = 0 deg from north) with the N1.8 camera during the nights of 20 April 2014 and 10 January 2015. We used the grating 150_$K_s$ ($R$ = 4140) for the $z > 3$ quasars and the grating 210_$zJHK$ ($R$ = 7838) in the $H$ band for J1549+1245 ($z \sim 2.4$). The average seeing during the observations was ∼0.7–0.8 arcsec for Cycle 2014 and ∼0.9–1.0 arcsec for Cycle 2015 (see Table 2). The spectra of telluric standards (A0V–A1V stellar types, see Table 2) were acquired immediately before/after the quasar.

Data were reduced using standard IRAF packages in combination with IDL tasks. The two-dimensional (2D) wavelength calibration was carried out on each frame of the five targets using argon and neon lamp exposures for J0745+4734 and J0900+4215, argon and xenon lamp exposures for J1549+1245, and sky emission lines for J1201+1206 and J1326−0005. The sky background subtraction was performed using the nodding technique. From the 2D calibrated and sky lines free spectra, we extracted one-dimensional (1D) spectra for both target and telluric standard star. As a final step, the flux calibration and telluric absorption correction were applied to the 1D spectra using the IDL based routine XTELLCOR_GENERAL (Vacca et al. 2003). This routine employs a high-resolution spectrum of Vega, convolved with the instrumental resolution, to fit both telluric and stellar features in the standard star spectrum to compute the telluric absorption correction for the quasar spectrum. The flux calibration, as a function of wavelength, was performed by a response curve based on the telluric standard $B$ and $V$ magnitudes, including the reddening curve of Rieke & Lebofsky (1985).

## 4. Analysis

### 4.1. Spectral analysis

Given the complexity of the spectra (see Fig. 1), data analysis was performed using IDL custom processing scripts. In order to reproduce the observed spectral features, we developed a suite of models based on the IDL package MPFIT (Markwardt 2009). Continuum and emission lines (H$\beta$, [OIII] and FeII) were simultaneously fitted by minimising the $\chi^2$. The statistical noise associated with the LUCI1 spectra is small (as WISSH quasars are near-IR bright sources) with respect to the systematics, e.g. the dispersion error associated with the grism. Therefore, we estimated the statistical noise from the line-free continuum emission and assumed it to be constant over the entire spectral range. We tested different spectral models to find the most appropriate description of the spectrum for each WISSH quasar. Specifically, all the spectra were fitted with the following models:

*Model A*, which consists of one Gaussian profile for fitting each component of the [OIII]$\lambda$4959, 5007 Å doublet; one Gaussian profile for fitting the H$\beta$ emission from the narrow-line region (NLR); and one broken power law, convolved with a Gaussian curve, for fitting the broad-line region (BLR) H$\beta$ emission (e.g. Nagao et al. 2006; Carniani et al. 2015).

*Model B1*, which includes one Gaussian profile for fitting each component of the narrow, systemic [OIII] doublet and one Gaussian profile to account for the NLR H$\beta$ emission; one Gaussian profile for fitting each component of the broad [OIII] doublet associated with the outflowing gas, and one Gaussian profile for fitting the corresponding broad H$\beta$ emission; and a broad Gaussian component for fitting the BLR H$\beta$ emission.

*Model B2*, which is similar to Model B1, except for a broken power-law profile, convolved with a Gaussian curve, included to describe the BLR H$\beta$ emission.

For both narrow and broad emission, the separation between each component of the [OIII]$\lambda$4959, 5007 Å doublet was fixed to 48 Å in the rest frame with a ratio of their normalisations equal to 1:3. Moreover, the standard deviation ($\sigma$) of the two doublet components was forced to be the same. For narrow(broad) H$\beta$ emission, the separation with respect to the narrow(broad) [OIII]$\lambda$5007 Å emission was fixed to 146 Å in the rest frame (assuming the same $\sigma$ of the [OIII] emission). All models include a power-law continuum component that is estimated from

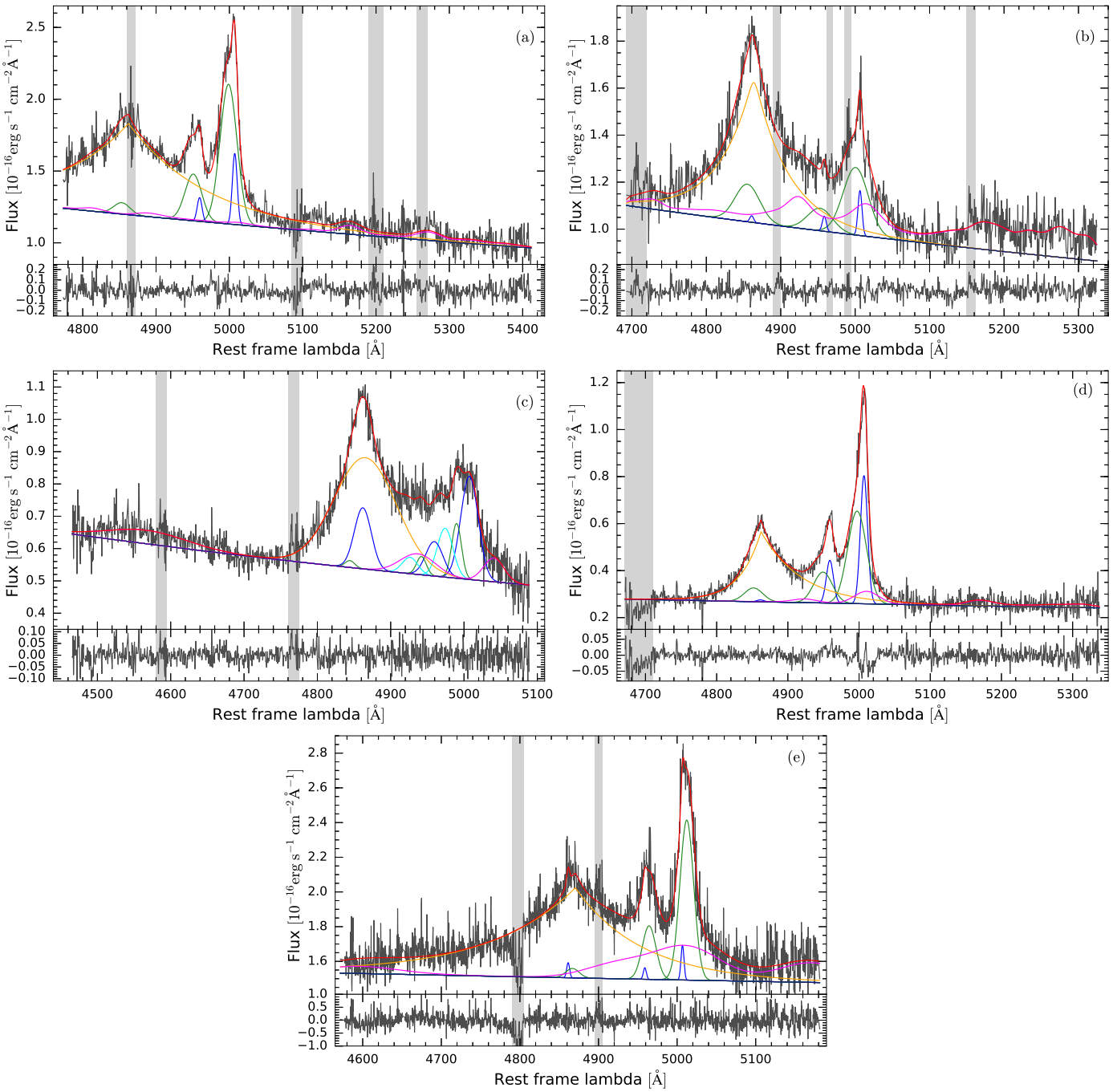


**Fig. 1.** LUCI1 spectra of the five analysed WISSH quasars. The red lines show the resulting best fits for **a)** SDSS J0745+4734, **b)** J0900+4215, **c)** J1201+1206, **d)** J1326−0005, and **e)** J1549+1245. Blue and green curves refer to the NLR core and broad emission of both [OIII] and H$\beta$, respectively. BLR H$\beta$ emission is indicated in orange and FeII emission is indicated in magenta. The cyan curve in panel **c)** represents the additional components necessary to account for the *plateau*-like emission feature between 4900–5000 Å in J1201+1206. Grey bands indicate the regions excluded from the fit because of the presence of telluric features.

feature-free spectral regions at both sides of the H$\beta$−[OIII] emission lines (except for J0745+4734, in which the spectral region bluewards the H$\beta$ is not observed), which are sufficiently wide (from ∼200 Å to ∼300 Å in the rest frame in case of J1201+1206 and J1326−0005, respectively) to enable a meaningful constraint and FeII emission.

Specifically, the complex FeII emission in the spectra was taken into account by adding to the fit a specific template based on observational FeII emission templates (Boroson & Green 1992; Véron-Cetty et al. 2004; Tsuzuki et al. 2006) or synthetic FeII spectral templates created by the Cloudy plasma simulation code (Ferland et al. 2013). Furthermore, by convolving these templates with a Gaussian function with a $\sigma$ value ranging from 1000 to 4000 km s$^{-1}$, we created a library of FeII emission templates for each quasar. In this way, we are able to describe the FeII emission in all our targets (see Fig. 1) but J1201+1206, for which we cannot find an appropriate FeII template. Accordingly, we decided to include in the fitting models of J1201+1206 three broad Gaussian components to account for the strong emission features observed at ∼4500, 4940, and 5040 Å, respectively. We

note that the widely used Boroson & Green (1992) template fails to provide a satisfactory fit to the FeII emission in all spectra.

In case of J1201+1206, A and B models are not able to account for the plateau-like emission feature in the 4900−4970 Å range (see Fig. 1c). Accordingly, the LUCI1 spectrum of this source were also fitted by the following models:

*Model C1*, which is similar to Model B2, but also includes an additional Gaussian profile to account for an extra broad component of [OIII]$\lambda$5007 Å, [OIII]$\lambda$4959 Å, and H$\beta$ emissions.

*Model C2*, which is similar to Model C1, but includes a broken power-law component, convolved with a Gaussian curve, to account for the BLR H$\beta$ emission.

### 4.2. Extinction estimate

The SEDs of the WISSH quasars were derived by fitting the near-UV to mid-IR photometric data (listed in Table 1) with a set of SED models created from the Type 1 AGN SED templates of Richards et al. (2006) and applying a SMC extinction law (Prevot et al. 1984) with colour excess $E(B-V)$ as free parameter. The detailed description of this procedure and the corresponding results for the entire WISSH quasars sample will be provided in a forthcoming paper (Duras et al.). The SMC-like extinction curve was used as usual for mildly reddened quasars up to $z \sim 2.5$ (e.g. Richards et al. 2003; Hopkins et al. 2004). Nonetheless, an additional SED fitting was tested by adopting the mean extinction curve (MEC) from Gallerani et al. (2010), which was found to be more representative of high-$z$ quasars ($z \sim 4-6$). The MEC extinction law was derived for $\lambda < 5000$ Å (Gallerani et al. 2010). For $\lambda > 5000$ Å, the dust extinction was accounted for by considering the curve from Calzetti et al. (2000), which is also widely used to estimate the reddening in high-$z$ objects (e.g. Lusso et al. 2012, for the COSMOS sample). The $E(B-V)$ values derived using the SMC or MEC+Calzetti extinction curve were found to be consistent within one standard deviation for all sources. Accordingly, the extinction level does not strongly depend on the adopted extinction curve, and we consider the SMC based values as reliable for our targets.

We find that J0745+4734 and J0900+4215 are compatible with no extinction while, for the remaining objects, we verified that by applying the SED-based $E(B-V)$ values to the typical intrinsic Type 1 quasar spectrum, provided by Vanden Berk et al. (2001), we are able to reproduce the observed LUCI1 and SDSS spectrum of each quasar. The spectra of J1201+1206 and J1549+1245 are successfully reproduced with $E(B-V) = 0.005$ and 0.148, respectively. In case of J1326−0005, the spectral template modified by the SED-based $E(B-V) = 0.296$ fails to describe the SDSS spectrum at $\lambda < 1200$ Å (rest frame). Specifically, the template rapidly drops at shorter wavelengths, while the observed spectrum remains almost flat down to ∼800 Å. There are two possible explanations for this: first, the SMC extinction curve is not appropriate to describe the extinction for this quasar; and, second, a contamination from the host galaxy emission can be present, in addition to the quasar emission, producing an excess in this wavelength range.

The application of the extinction curves from Calzetti et al. (2000) and Gallerani et al. (2010) have not successfully reproduced the observed spectrum. We have therefore added in the SED fitting model a host galaxy component chosen among the templates of Bruzual & Charlot (2003), obtaining an excellent description of the data. Accordingly, we assume the SED-based $E(B-V) = 0.296$ for J1326−0005.

## 5. Results

### 5.1. Best-fit models

The rest-frame main spectral parameters, derived from the different models applied to the LUCI1 data, are shown in Table 3. In the following, the quoted errors refer to one standard deviation confidence level. The FWHM values are not corrected for instrumental broadening, as they are much broader than the LUCI1 spectral resolution (rest-frame $FWHM_{\rm ins} \lesssim 20$ km s$^{-1}$).

*SDSS J0745+4734*: the LUCI1 spectrum of this WISSH quasar exhibits a prominent, well-defined [OIII] doublet emission emerging from the extended red wing of the H$\beta$ profile, as shown in Fig. 1a. The best-fit description of this spectrum is provided by Model B2 with an associated $\chi^2_\nu = 1.27$.
It is possible to accurately constrain the weak FeII emission underlying the [OIII] region thanks to the spectral coverage extended up to ∼5400 Å. Two Gaussian components are necessary to properly reproduce the skewed [OIII] emission profile, dominated by a blueshifted, broad (i.e., $FWHM^{\rm broad}_{\rm [OIII]} \sim 1630$ km s$^{-1}$) component. The ratio between the integrated flux of the broad [OIII] component, centred at ∼4999 Å, and the core ($FWHM^{\rm core}_{\rm [OIII]} \sim 470$ km s$^{-1}$) component is ∼6.8. The H$\beta$ emission is characterised by a very large profile, with a $FWHM^{\rm BLR}_{\rm H\beta} \sim 8600$ km s$^{-1}$, i.e. the highest value derived within our sample.

*SDSS J0900+4215*: the LUCI1 spectrum of this quasar is dominated by the H$\beta$ emission and shows a strong FeII pseudo-continuum (Fig. 1b). Model B2 yields the best-fit for this spectrum ($\chi^2_\nu = 1.57$).
The [OIII] emission is best fitted by two Gaussian components, i.e. a narrow ($FWHM^{\rm core}_{\rm [OIII]} \sim 300$ km s$^{-1}$) component representing the systemic emission, and an extremely broad ($FWHM^{\rm broad}_{\rm [OIII]} \sim 2240$ km s$^{-1}$) and blueshifted component with centroid $\lambda^{\rm broad}_{\rm OIII} \sim 4999$ Å. The broad [OIII] component dominates the emission with a [OIII]$^{\rm broad}$/[OIII]$^{\rm core}$ flux ratio of ∼12. The skewed H$\beta$ profile is better reproduced by a broken power law. We derive a $FWHM^{\rm BLR}_{\rm H\beta} \sim 3200$ km s$^{-1}$, which is the lowest value in our sample.

*SDSS J1201+1206*: the most striking feature in the LUCI1 spectrum of this quasar is the *plateau*-like emission ranging redwards the peak of the strong H$\beta$ emission up to the peak of the [OIII]$\lambda$5007 Å, which Models A and B are not able to account for (see Fig. 1c and Sect. 4.1). We therefore applied to the data models C1 and C2, which include three Gaussian profiles for each component of the [OIII] doublet, to reproduce the broad/complex [OIII] emission. Model C1 yields the best description of the spectrum with an associated $\chi^2_\nu = 1.26$ (see Table 3).
The bulk of the [OIII] emission comes from a broad Gaussian line centred at 5007 Å, with a FWHM of ∼1700 km s$^{-1}$. Such a high value clearly indicates that this line cannot be ascribed to the NLR, but it is associated with high-velocity, outflowing gas, and suggests degeneracy between the Gaussian profiles used in the model to fit the [OIII] emission. The H$\beta$ emission is best fitted by the combination of three Gaussian profiles. The FWHM of the BLR H$\beta$ line results ∼6200 km s$^{-1}$. J1201+1206 is also characterised by emission features likely associated with FeII, which is relevant in the region bluewards the H$\beta$ and in correspondence of the *plateau*-like feature.

**Table 3.** Spectral fit results derived from the different models (see Sect. 4.1) applied to (a) SDSS J0745+4734; (b) J0900+4215; (c) J1201+1206; (d) J1326−0005; and (e) J1549+1245. Boldface indicates the best-fit model.

(a) SDSS J0745+4734 $z_{\rm spec} = 3.225 \pm 0.001$

| Parameter | Mod A | Mod B1 | **Mod B2** | Units |
|---|---|---|---|---|
| $\chi^2_\nu$ | 1.46 | 1.30 | 1.27 | |
| $\mathrm{FWHM}^{\rm core}_{\rm [OIII]}$ | 1510 ± 160 | 440 ± 150 | 470 ± 170 | km s$^{-1}$ |
| $\mathrm{FWHM}^{\rm broad}_{\rm [OIII]}$ | – | 1740 ± 170 | 1630 ± 180 | km s$^{-1}$ |
| $\lambda^{\rm broad}_{\rm [OIII]}$ | – | 4999 ± 1 | 4999 ± 1 | Å |
| Flux [OIII]$^{\rm broad}$/ [OIII]$^{\rm core}$ | – | 8.5 ± 1.6 | 6.8 ± 1.3 | |
| $\lambda^{\rm BLR}_{\rm H\beta}$ | 4866 ± 2 | 4867 ± 3 | 4862 ± 1 | Å |
| $\mathrm{FWHM}^{\rm BLR}_{\rm H\beta}$ | 6920 ± 210 | 8130 ± 230 | $8600^{+230}_{-200}$ | km s$^{-1}$ |
| Flux H$\beta^{\rm BLR}$/H$\beta^{\rm Tot}$ | $0.99^{+0.01}_{-0.05}$ | 0.93 ± 0.06 | $0.98^{+0.02}_{-0.08}$ | |

(b) SDSS J0900+4215 $z_{\rm spec} = 3.294 \pm 0.001$

| Parameter | Mod A | Mod B1 | **Mod B2** | Units |
|---|---|---|---|---|
| $\chi^2_\nu$ | 1.95 | 1.65 | 1.57 | |
| $\mathrm{FWHM}^{\rm core}_{\rm [OIII]}$ | 2030 ± 180 | 250 ± 130 | 300 ± 130 | km s$^{-1}$ |
| $\mathrm{FWHM}^{\rm broad}_{\rm [OIII]}$ | – | 2340 ± 270 | 2240 ± 170 | km s$^{-1}$ |
| $\lambda^{\rm broad}_{\rm [OIII]}$ | – | 5004 ± 3 | 4999 ± 1 | Å |
| Flux [OIII]$^{\rm broad}$/ [OIII]$^{\rm core}$ | – | 19.1 ± 3.3 | 11.7 ± 1.8 | |
| $\lambda^{\rm BLR}_{\rm H\beta}$ | 4867 ± 2 | 4871 ± 3 | 4861 ± 1 | Å |
| $\mathrm{FWHM}^{\rm BLR}_{\rm H\beta}$ | 3740 ± 210 | 6900 ± 280 | 3210 ± 190 | km s$^{-1}$ |
| Flux H$\beta^{\rm BLR}$/H$\beta^{\rm Tot}$ | 0.93 ± 0.05 | $0.92^{+0.03}_{-0.06}$ | 0.98±0.02 | |

(c) SDSS J1201+1206 $z_{\rm spec} = 3.512 \pm 0.002$

| Parameter | Mod A | **Mod C1** | Mod C2 | Units |
|---|---|---|---|---|
| $\chi^2_\nu$ | 1.41 | 1.26 | 1.30 | |
| $\mathrm{FWHM}^{\rm broad,5007\ Å}_{\rm [OIII]}$ | (2560 ± 200 | 1670 ± 190 | 1700 ± 200)$^a$ | km s$^{-1}$ |
| $\mathrm{FWHM}^{\rm broad,shifted}_{\rm [OIII]}$ | – | 940 ± 210 | 960 ± 180 | km s$^{-1}$ |
| | | $(1510^{+300}_{-180}$ | 1700 ± 280)$^b$ | |
| $\lambda^{\rm broad,shifted}_{\rm [OIII]}$ | – | 4990 ± 2 | 4989 ± 2 | Å |
| | | (4970 ± 1 | 4973 ± 2)$^b$ | |
| $\lambda^{\rm BLR}_{\rm H\beta}$ | 4867 ± 3 | 4865 ± 2 | 4858 ± 2 | Å |
| $\mathrm{FWHM}^{\rm BLR}_{\rm H\beta}$ | 7470 ± 280 | 6160 ± 250 | 4800 ± 200 | km s$^{-1}$ |
| Flux H$\beta^{\rm BLR}$/H$\beta^{\rm Tot}$ | $0.92^{+0.08}_{-0.10}$ | 0.86±0.07 | $0.96^{+0.04}_{-0.1}$ | |

(d) SDSS J1326−0005 $z_{\rm spec} = 3.303 \pm 0.001$

| Parameter | Mod A | Mod B1 | **Mod B2** | Units |
|---|---|---|---|---|
| $\chi^2_\nu$ | 2.42 | 1.81 | 1.51 | |
| $\mathrm{FWHM}^{\rm core}_{\rm [OIII]}$ | 1290 ± 160 | 730 ± 160 | 710 ± 170 | km s$^{-1}$ |
| $\mathrm{FWHM}^{\rm broad}_{\rm [OIII]}$ | – | 1980 ± 170 | 1870 ± 170 | km s$^{-1}$ |
| $\lambda^{\rm broad}_{\rm [OIII]}$ | – | 4997 ± 1 | 4997 ± 1 | Å |
| Flux [OIII]$^{\rm broad}$/ [OIII]$^{\rm core}$ | – | 1.9 ± 1.0 | 1.9 ± 0.9 | |
| $\lambda^{\rm BLR}_{\rm H\beta}$ | $4865^{+1}_{-3}$ | 4874 ± 2 | 4862 ± 1 | Å |
| $\mathrm{FWHM}^{\rm BLR}_{\rm H\beta}$ | $5480^{+250}_{-200}$ | $5520^{+180}_{-240}$ | 3700 ± 160 | km s$^{-1}$ |
| Flux H$\beta^{\rm BLR}$/H$\beta^{\rm Tot}$ | 0.92 ± 0.06 | 0.8±0.1 | $0.93^{+0.07}_{-0.09}$ | |

(e) SDSS J1549+1245 $z_{\rm spec} = 2.365 \pm 0.001$

| Parameter | Mod A | Mod B1 | **Mod B2** | Units |
|---|---|---|---|---|
| $\chi^2_\nu$ | 1.45 | 1.42 | 1.37 | |
| $\mathrm{FWHM}^{\rm core}_{\rm [OIII]}$ | 1260 ± 210 | 280 ± 160 | 270 ± 160 | km s$^{-1}$ |
| $\mathrm{FWHM}^{\rm broad}_{\rm [OIII]}$ | – | 1250 ± 210 | 1240 ± 210 | km s$^{-1}$ |
| $\lambda^{\rm broad}_{\rm [OIII]}$ | – | 5012 ± 1 | 5012 ± 1 | Å |
| Flux [OIII]$^{\rm broad}$/ [OIII]$^{\rm core}$ | – | 20±2 | 21 ± 3 | |
| $\lambda^{\rm BLR}_{\rm H\beta}$ | 4864 ± 2 | 4882 ± 2 | 4871 ± 2 | Å |
| $\mathrm{FWHM}^{\rm BLR}_{\rm H\beta}$ | 7810 ± 250 | $11\,100^{+310}_{-260}$ | 8340 ± 280 | km s$^{-1}$ |
| Flux. H$\beta^{\rm BLR}$/H$\beta^{\rm Tot}$ | $0.98^{+0.02}_{-0.10}$ | $0.94^{+0.06}_{-0.09}$ | $0.98^{+0.02}_{-0.09}$ | |

**Notes.** The spectroscopic redshift for each WISSH quasar, estimated from the best fit of LUCI1 data, is also shown. $^{(a)}$ Values derived for the broad [OIII] component at 5007 Å (see Sect. 5.1). $^{(b)}$ Values derived for the additional broad, shifted [OIII] component included in models C1 and C2 (see Sect. 4.1).

*SDSS J1326-0005*: the LUCI1 spectrum of this WISSH quasar (see Fig. 1d) resembles that typically observed for less luminous quasars, with a very prominent [OIII] emission with respect to the H$\beta$ emission. Model B2 provides a good description of the LUCI1 spectrum with an associated reduced $\chi^2_\nu = 1.51$.
Two Gaussian components are needed to properly reproduce the broad and skewed profile of the [OIII] emission. The core component shows a $\mathrm{FWHM}^{\mathrm{core}}_{[\mathrm{OIII}]}$ of $\sim$700 km s$^{-1}$, while the broad component is centred at 4997 ± 1 Å, with a $FWHM^{\mathrm{broad}}_{[\mathrm{OIII}]} \sim 1900$ km s$^{-1}$. The ratio between the flux of broad and core component is $\sim$1.9. The H$\beta$ emission is dominated by the contribution from the BLR and, because of the highly skewed and asymmetric profile, cannot be reproduced by a Gaussian function and requires the application of a broken power-law component, for which we measure a $FWHM^{\mathrm{BLR}}_{\mathrm{H}\beta} \sim 3700$ km s$^{-1}$.

*SDSS J1549+1245*: the *H*-band spectrum of J1549+1245 is characterised by a very broad ($FWHM^{\mathrm{BLR}}_{\mathrm{H}\beta} \sim 8300$ km s$^{-1}$) H$\beta$ profile (see Fig. 1e), similar to the J0745+4734 spectrum. The [OIII] doublet clearly emerges from the very extended H$\beta$ red wing. Model B2 provides the best-fit model for this quasar ($\chi^2_\nu = 1.37$).
The prominent H$\beta$ line makes an accurate fitting of the [OIII] emission difficult, as part of it (in particular the broad wings) is likely blended in the H$\beta$ profile (similar to the underlying FeII emission). Nonetheless, two Gaussian components are necessary to properly reproduce the [OIII] emission, where the broad component (i.e. $FWHM^{\mathrm{broad}}_{[\mathrm{OIII}]} \sim 1240$ km s$^{-1}$) is much stronger than the core emission. The centroid of the broad Gaussian is at 5012 ± 1 Å, indicating that the bulk of the [OIII] emission is associated with receding material.

Table 3 lists the spectroscopic redshift of our sources derived from the best-fit model. Our estimates significantly (>3$\sigma$) differ from the SDSS redshifts (see Table 1), which are based on UV emission lines and derived by an automatic procedure. J0900+4215 is the only source for which we find a $z_{\mathrm{spec}}$ value comparable to $z_{\mathrm{SDSS}}$.

We derived an additional redshift estimate of our targets from the CIV line detected in the SDSS spectra. The CIV-based redshifts are systematically lower (with blueshifts $\lesssim$800 km s$^{-1}$) than those derived from the H$\beta$ line, except for J1326−0005, which does not show any significant shift (details on the CIV emission line properties and blueshifts in WISSH quasars will be discussed in a forthcoming paper by Vietri et al.).

### 5.2. Two-dimensional and "off-nuclear" spectra

The presence of ionised, extended emitting gas can be investigated by extracting 1D spectra, at increasing offset distances from the central position, from the 2D spectrum that was obtained with the 1 arcsec slit with PA = 0 deg. In fact, moving away from the centre, we expect a reduced contamination from the nuclear emission and, therefore, possible spatially extended [OIII] features should be enhanced (Perna et al. 2015a). This approach can provide useful hints about emission components roughly oriented along the slit.

First, for each quasar, we extracted the spectrum from an aperture of 2 pixels, i.e. the [−1, 1] spectrum of the [−1, 0] and [0, 1] pixels with 1 pixel corresponding to 0.25 arcsec and $\sim$2 kpc at the redshifts of our targets, centred on the peak of the spatial profile of the continuum emission. Figure 2a shows the case for J1201+1206, while the 2D spectra of the remaining quasars can be found in the Appendix. Negative (positive) pixel values correspond to the north (south) direction. Spectra from apertures of 1 pixel width were then extracted to study the "off-nuclear" spectra at increasing distance from the central peak, both in the south and north direction, as far as the spectra were not too noisy to derive meaningful results. For each 1D spectrum we carried out a detailed analysis that is similar to that performed for the integrated spectrum (see Sect. 4.1), as shown in Fig. 2 for the quasar J1201+1206.

Moreover, to trace any additional extended feature not ascribed to the nuclear emission, we calculated the ratio between the integrated flux of the [OIII] and BLR H$\beta$ emission for each aperture. Since the BLR H$\beta$ traces the nuclear emission, an increase of the relative strength of the [OIII] component with respect to the BLR H$\beta$ cannot be due to contamination from nuclear emission and, therefore, indicates the presence of truly extended emission. This has highlighted evidence of possible extended [OIII] emission in three out of five sources, namely J0745+4734, J1201+1206, and J1326−0005. In this section, we present and discuss in detail the results obtained for J1201+1206, while the results for the remaining sources are presented in the Appendix.

J1201+1206 shows a very complex scenario with extended [OIII] emission characterised by blueshifted and redshifted components, which are likely to be associated with a bipolar outflow. The "off-nuclear" flux-calibrated spectra, extracted along south and north direction, together with their multi-component fits, are shown in Figs. 2b and c, respectively. As expected, the signal-to-noise ratio significantly decreases in the outer apertures. All "off-nuclear" spectra show broad H$\beta$ emission line, indicating that none of the spectra are totally free from nuclear contamination. However, blueshifted and redshifted emission features, related to extended [OIII], clearly emerge in addition to the nuclear light. Furthermore, [OIII] emission up to $\sim$5 kpc is characterised by the presence of a broad component, centred at 5007 Å, similar to the profile found in the integrated spectrum (see Fig. 1c and Sect. 5.1).

More specifically, Fig. 2b shows the presence of an emission line at $\sim$4993 Å along south direction, interpreted as blueshifted [OIII], and visible at distance up to $\sim$5–7 kpc (i.e. in the [−4, −3] and [−5, −4] spectra). On the contrary, a prominent emission line redwards of 5007 Å, i.e. centred at $\sim$5017 Å, clearly emerges in all spectra from the north side up to $\sim$7 kpc (Fig. 2c). This redshifted [OIII] emission component might be interpreted as the red wing of the broad ($FWHM \sim 1700$ km s$^{-1}$) [OIII] line detected in the integrated spectrum at 5007 Å (Fig. 1c). In Fig. 3a, we plot the velocity shift $\Delta v$ of the blue- and redshifted [OIII] component at different apertures with respect to 5007 Å. The velocity shift between the blueshifted and redshifted [OIII] emission is $\sim$1500 km s$^{-1}$. Such a value cannot be explained in terms of rotation, as it is a factor of $\gtrsim$4 larger than the typical value observed for a $z \sim 2$–3 galaxy (Bouché et al. 2007). Furthermore, it would imply a very high mass enclosed within 7 kpc, i.e. $\sim 4 \times 10^{12}\ M_\odot$. The bipolar outflow scenario can be therefore considered as the most likely explanation for the velocity shift observed in J1201+1206.

Figure 3b shows the integrated flux ratio between the two [OIII] components (i.e. the broad component at 5007 Å and the blue/redshifted component) and the BLR H$\beta$ emission as a function of the aperture. The broad [OIII] emission component

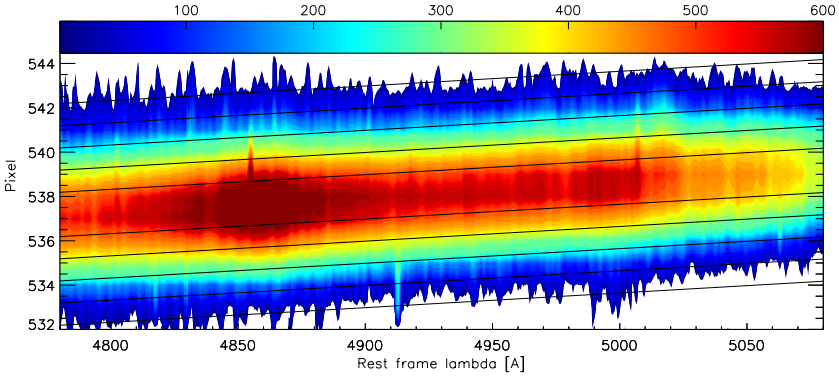


(a)

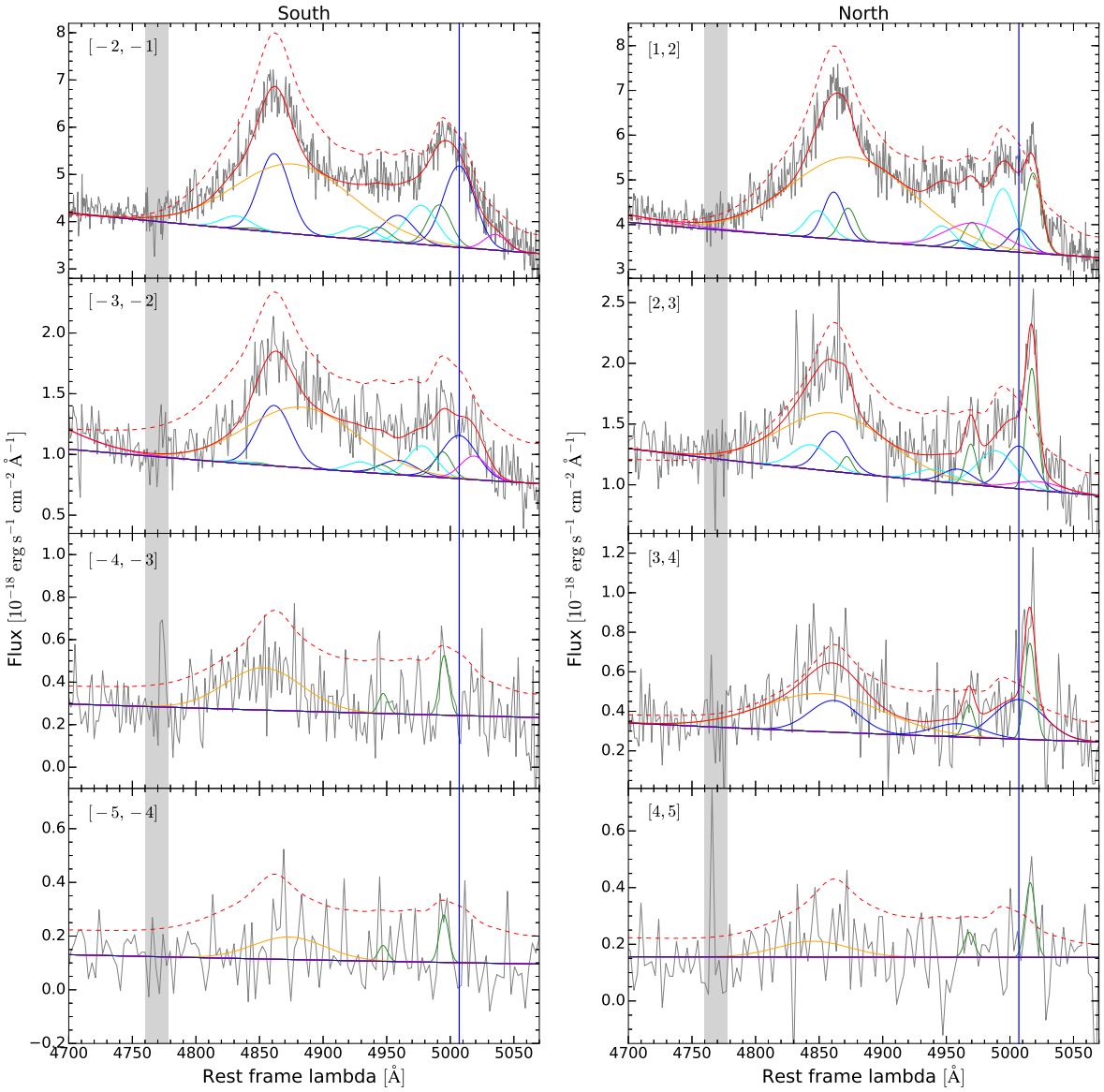


(b) (c)

**Fig. 2. a)** 2D LUCI1 spectrum of J1201+1206. Blue to red colours indicate increasing counts. Since the LUCI1 spectra were acquired with PA = 0 deg, the top and bottom correspond to north and south directions, respectively. The black solid lines indicate the apertures used for extracting the off-nuclear spectra. Panels **b)** and **c)** show the "off-nuclear" spectra of J1201+1206 extracted in 1 pixel (∼1.9 kpc) width regions at increasing distances from the peak of the spatial profile of the continuum emission. Negative (positive) pixel values correspond to south (north) direction. In both panels, the offset increases from *top to bottom*, as indicated by the corresponding pixels interval. Spectral components are indicated as in Fig. 1c. The vertical line corresponds to $\lambda$ = 5007 Å, while the dashed red line indicates the best-fit model of the central spectrum extracted from the two-pixels region [−1, 1], plotted with arbitrary normalisation for display purpose only. Grey bands indicate the regions excluded from the fit because of the presence of telluric features.

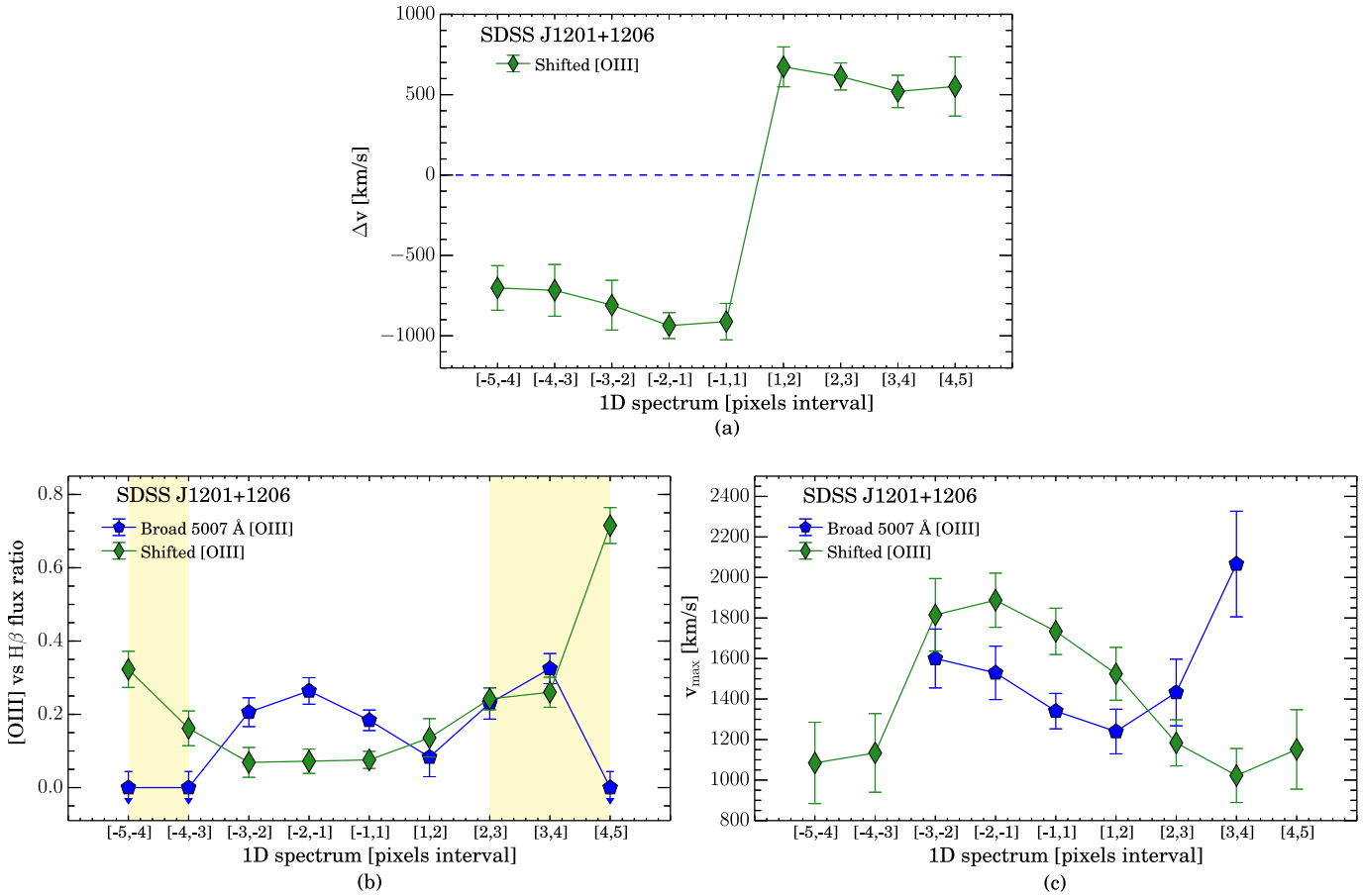


**Fig. 3. a)** Velocity shift of the blue- and redshifted [OIII] component with respect to 5007 Å (dashed line), detected in the "off-nuclear" spectra of J1201+1206 extracted from different apertures. Negative(positive) pixel values correspond to south(north) direction (1 pixel ∼1.9 kpc at the redshift of J1201+1206). **b)** The ratio between the integrated flux of the two [OIII] components (i.e. the broad component at 5007 Å and the blue- and redshifted component) and the BLR H$\beta$ emission for the "off-nuclear" spectra of J1201+1206. The yellow bands highlight the presence of extended [OIII] emission. **c)** Maximum velocity of the broad [OIII] component at 5007 Å and the blue- and redshifted [OIII] component detected in the "off-nuclear" spectra of J1201+1206.

is not observed at distances larger than 3 pixels from the central position, while the relative strength of the blue- and redshifted component increases with distance, implying the presence of an extended outflow. The maximum velocity of these two [OIII] components, defined as $v_{\rm max} = |\Delta v| + 2\sigma$, derived from each "off-nuclear" spectrum is plotted in Fig. 3c, indicating that both components are associated with outflowing ($v_{\rm max} > 1000$ km s$^{-1}$) ionised gas.

The extended [OIII] emission revealed in the other two quasars, i.e. J0745+4734 and J1326−0005, shows a different spatial behaviour. As for J0745+4734, we have hints of systemic, narrow [OIII] emission extended in the south direction, at a distance of 6–8 pixels (i.e. ∼11–13 kpc), provided by an increase of the ratio between the integrated flux of the [OIII]$\lambda$5007 Å and the BLR H$\beta$ component (see Fig. A.1). The analysis of the "off-nuclear" spectra of J1326−0005 has allowed us to detect extended outflowing ($v_{\rm max} \sim 1300$ km s$^{-1}$) [OIII] emission in the north direction up to a distance of ∼9 kpc (see Fig. A.3). Finally, the low signal-to-noise ratio of the "off-nuclear" spectra extracted for J0900+4215 and 1549+1245 hampers us from inferring any firm conclusion on the presence of extended emission around these quasars.

### 5.3. H$\beta$-based SMBH masses and Eddington ratios

The virial mass of the central SMBH ($M_{\rm BH}^{H\beta}$) for our WISSH quasars has been derived from the FWHM of the BLR H$\beta$. The latter has been demonstrated to be a more reliable single-epoch SMBH mass estimator than CIV FWHM (Baskin & Laor 2005; Shen & Liu 2012), which has been adopted for the calculation of the $M_{\rm BH}$ of WISSH quasars in Weedman et al. (2012). More specifically, we used the FWHM$_{\rm H\beta}^{\rm BLR}$ values derived from the best fits (see Table 3), the intrinsic luminosity at 5100 Å, $\lambda L_\lambda$(5100 Å), obtained from broadband (mid-IR to UV) SED fitting (Duras et al., in prep., see Table 4), and the empirical BLR size–luminosity relation reported in Bongiorno et al. (2014), i.e.

$$\mathrm{Log}(M_{\rm BH}^{\rm H\beta}/M_\odot) = 6.7 + 2\mathrm{Log}\left(\frac{FWHM_{\rm H\beta}}{10^3\ \mathrm{km\ s^{-1}}}\right) + 0.5\mathrm{Log}\left(\frac{\lambda L_\lambda(5100\ \text{Å})}{10^{44}\ \mathrm{erg\ s^{-1}}}\right). \quad (1)$$

The resulting $M_{\rm BH}^{\rm H\beta}$ values for the WISSH quasars, ranging from $\sim 2\times10^9\ M_\odot$ up to $\sim 1.6\times10^{10}\ M_\odot$, are shown in Table 4 and indicate that our targets populate the massive end of the black hole mass function at $z \sim 2.5$–$3.5$ (Kelly & Merloni 2012). Table 4

**Table 4.** Luminosity at 5100 Å, bolometric luminosity, SMBH mass, and Eddington ratio of the five WISSH quasars.

| SDSS (1) | $\lambda L_{5100\,Å}$ (2) | $L_{Bol}$ (3) | $M_{BH}^{H\beta}$ (4) | $M_{BH}^{CIV}$ (5) | $\lambda_{Edd}$ (6) |
|---|---|---|---|---|---|
| J0745+4734 | 1.8 | 10.0 | $15.7 \pm 2.1$ | $8.7 \pm 0.5$ | $0.5 \pm 0.1$ |
| J0900+4215 | 1.7 | 8.3 | $2.1 \pm 0.3$ | $6.6 \pm 0.4$ | $3.1 \pm 0.5$ |
| J1201+1206 | 1.2 | 5.9 | $6.5 \pm 0.6$ | $6.2 \pm 0.2$ | $0.7 \pm 0.1$ |
| J1326-0005 | 1.0 | 5.6 | $2.1 \pm 0.3$ | $0.11 \pm 0.02$ | $2.1^{+0.3}_{-0.6}$ |
| J1549+1245 | 1.3 | 6.5 | $12.6 \pm 2.2$ | $1.9 \pm 0.5$ | $0.4 \pm 0.1$ |

**Notes.** Columns give the following information: (1) SDSS ID; (2) intrinsic luminosity at 5100 Å (in units of $10^{47}$ erg s$^{-1}$); (3) bolometric luminosity (in units of $10^{47}$ erg s$^{-1}$); (4) H$\beta$-based SMBH mass (in units of $10^9$ $M_\odot$); (5) CIV-based SMBH mass (in units of $10^9$ $M_\odot$) listed in Weedman et al. (2012); and (6) Eddington ratio, as derived from our H$\beta$-based SMBH mass estimates. The error associated with the $M_{BH}^{H\beta}$ includes both the statistical uncertainties affecting the $\lambda L_\lambda$(5100 Å) and $FWHM_{H\beta}^{BLR}$ values and the systematic uncertainty in the virial relation itself (~0.3 dex; see Bongiorno et al. 2014, for a complete discussion).

also lists the SED-based bolometric luminosity and Eddington ratio $\lambda_{Edd} = L_{Bol}/L_{Edd}$. The WISSH quasars are accreting at a high rate with $\lambda_{Edd} \sim 0.4$–3. This further demonstrates that WISSH quasars clearly offer the opportunity to collect high-mass, highly accreting SMBHs in a redshift interval that corresponds to the peak of the quasar number density.

Apart from J1201+1206, the H$\beta$-based $M_{BH}^{H\beta}$ are significantly ($\gtrsim 3\sigma$) different from the $M_{BH}$ values derived from the CIV line in Weedman et al. (2012), which are also reported in Table 4. In case of J1326−0005 and J1549+1245, the big difference (larger than a factor of 6 up to 20) between the two estimates can be explained in terms of extinction (which is more effective for UV lines, see Sect. 4.2) or presence of a broad absorption line (Gibson et al. 2009), which strongly affects the CIV line profile measured in the SDSS spectrum.

Figure 4 shows the bolometric luminosity as a function of $M_{BH}^{H\beta}$ for the five WISSH quasars, compared with other AGN samples from the literature. Specifically, we used the sample of ~170 X-ray selected broad-line AGN in COSMOS (for which the $M_{BH}$ has been derived from H$\beta$ and MgII; Lusso et al. 2012) and ~100 optically bright, SDSS quasars with $\mathrm{Log}(L_{Bol}/\mathrm{erg\,s^{-1}}) \sim 46$–48 at $1.5 < z < 3.5$, obtained by merging the samples of Shen (2016) and Shemmer et al. (2004), which report H$\beta$-based SMBH masses. The location of WISSH quasars in the $L_{Bol}$–$M_{BH}^{H\beta}$ plane indicates that the WISE selection criterion provides a simple and valuable tool to complete the census of the extreme SMBH population in the Universe.

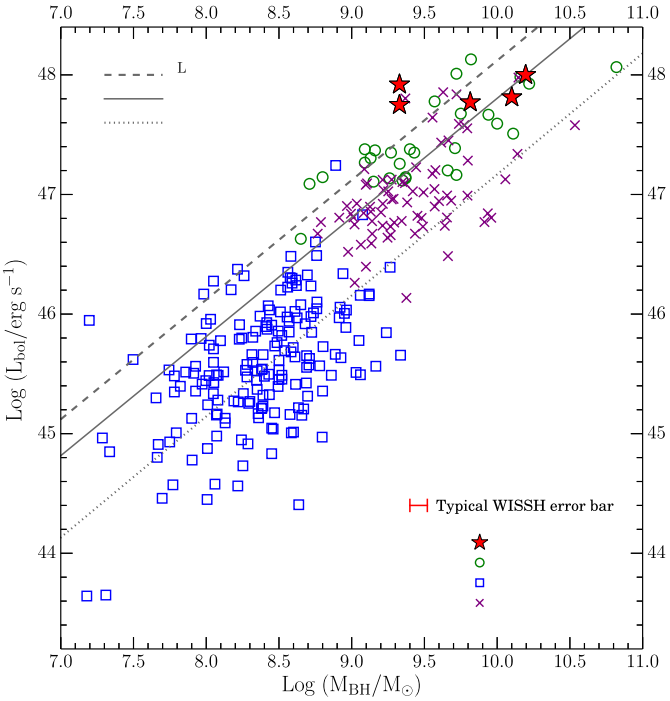


**Fig. 4.** Bolometric luminosity as a function of the H$\beta$-based SMBH mass ($M_{BH}^{H\beta}$) for different AGN samples. The WISSH quasars are indicated by red stars, while squares refer to X-ray selected Type 1 AGN from Lusso et al. (2012). Circles and crosses indicate the optically selected $z \sim 2$–3 quasars from Shemmer et al. (2004) and Shen (2016), respectively. The lines correspond to $L_{Bol}/L_{Edd} = 1$ (dashed), $L_{Bol}/L_{Edd} = 0.5$ (solid), and $L_{Bol}/L_{Edd} = 0.1$ (dotted).

## 6. Discussion

### 6.1. Properties of the broad [OIII] emission

All the five analysed WISSH quasars spectra show very broad [OIII] emission ($FWHM_{[OIII]}^{broad} \sim 1200$–2200 km s$^{-1}$; see Table 3). A systemic, core ($FWHM_{[OIII]}^{core} \lesssim 500$–700 km s$^{-1}$) [OIII] component, typically associated with emission from the NLR, is detected in all targets but J1201+1206. However, the $[OIII]_{broad}/[OIII]_{core}$ flux ratios ranging from 2 to 20 indicate that the bulk of the emission is provided by the broad component. In the case of J1201+1206, the emission line centred at 5007 Å exhibits a very large FWHM value (~1700 km s$^{-1}$) and, therefore, can be also considered as representative of outflow.

The broad, shifted [OIII] component is blueshifted in all cases except J1549+1245, for which a mildly redshifted ($\lambda_{[OIII]}^{broad} \sim 5012$ Å) broad component has been found. Fluxes and luminosities of the core and broad [OIII] emissions derived from the best fits of the LUCI1 spectra are shown in Table 5. In case of J1201+1206 we also list the values associated with the additional broad [OIII] component present in model C1 (see Sect. 4.1). The values of the intrinsic [OIII] luminosity were computed using the SMC extinction curve and the $E(B-V)$ values listed in Table 1 (see Sect. 4.2).

A comparison with previous studies on ionised outflows reveals that the WISSH quasars survey provides the opportunity to expand the explorable range of [OIII] luminosity up to ~$10^{45}$ erg s$^{-1}$. This is shown in Fig. 5, in which the FWHM of the broad [OIII] line is plotted versus the total observed [OIII]$\lambda$5007 Å luminosity ($L_{[OIII]}^{Tot}$). The WISSH quasars are compared with various AGN samples, including both Type 1 and Type 2 objects at low ($z < 1$) and high ($z > 1$) redshift. The WISSH quasars are located at the right-top corner of the plot, indicating that our selection allows us to extend the discovery of ionised outflows up to sources with observed $L_{[OIII]}^{Tot} \gtrsim 3 \times 10^{44}$ erg s$^{-1}$ up to ~$10^{45}$ erg s$^{-1}$ in case of J0745+4734. There is a hint that the $FWHM_{[OIII]}^{broad}$ increases with the [OIII] luminosity (Mullaney et al. 2013), while no redshift dependence seems to be present. More specifically, a lack of AGN with luminous [OIII] emission exhibiting a narrow (<1000 km s$^{-1}$) line profile is evident in the $FWHM_{[OIII]}^{broad}$–$L_{[OIII]}^{Tot}$ plane. This finding is further supported by the fact that in all other 13 WISSH quasars observed with LUCI1, the [OIII] emission is absent or very weak,

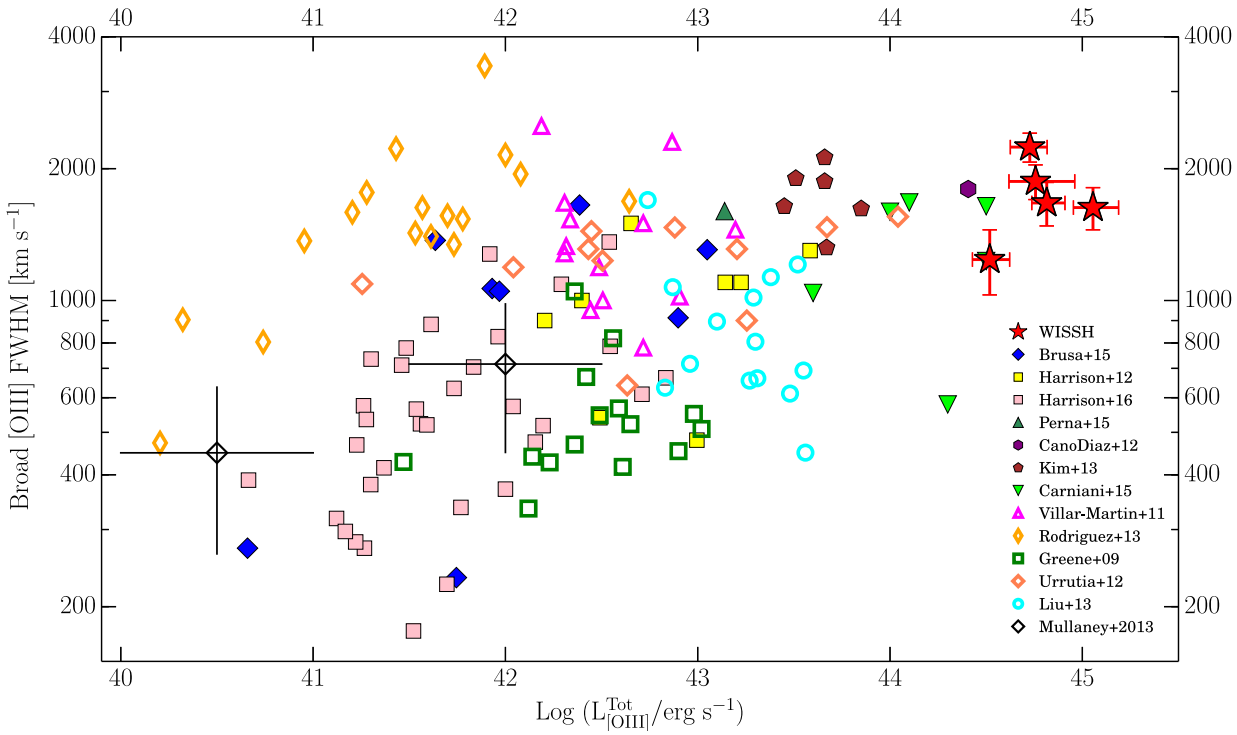


**Fig. 5.** FWHM$^{broad}_{[OIII]}$ as a function of the total observed [OIII]$\lambda$5007 Å luminosity ($L^{Tot}_{[OIII]}$) for different AGN samples. WISSH quasars (red stars) are compared with other samples of Type 1 and Type 2 AGN at low ($z < 1$, empty symbols) and high ($z > 1$, filled symbols) redshift. We plot the values obtained for a sample of obscured (Greene et al. 2009; Brusa et al. 2015; Perna et al. 2015a), red (Urrutia et al. 2012), Type 2 (Villar-Martín et al. 2011; Liu et al. 2013), luminous $z \sim 2.4$ (Cano-Díaz et al. 2012; Carniani et al. 2015), KASHz at $z \sim 1.1-1.7$ (Harrison et al. 2016), and radio quasars (Kim et al. 2013), and those obtained for the local and high-$z$ ULIRGs by Rodríguez Zaurín et al. (2013) and Harrison et al. (2012), respectively. The average values in two $L^{Tot}_{[OIII]}$ bins for optically selected Type 2 AGN in Mullaney et al. (2013) are also shown.

**Table 5.** Properties of the core and broad components of the [OIII] emission, as derived from the best fits of the LUCI1 spectra (see Sect. 3).

| SDSS | $F^{core}_{[OIII]}$<br>$F^{broad}_{[OIII]}$ | $L^{core}_{[OIII],obs}$<br>$L^{broad}_{[OIII],obs}$ | $L^{core}_{[OIII],int}$<br>$L^{broad}_{[OIII],int}$ |
|---|---|---|---|
| (1) | (2) | (3) | (4) |
| J0745+4734 | 1.8 ± 0.9 | 1.7 ± 0.8 | 1.7 ± 0.8 |
| | 11.9 ± 3.0 | 11.4 ± 2.9 | 11.4 ± 2.9 |
| J0900+4215 | $0.4^{+1.0}_{-0.2}$ | $0.5^{+1.0}_{-0.3}$ | $0.5^{+1.0}_{-0.3}$ |
| | 5.2 ± 1.0 | 5.3 ± 1.0 | 5.3 ± 1.0 |
| J1201+1206 | (4.3 ± 0.9 | 5.0 ± 1.0 | 5.0 ± 1.0)$^a$ |
| | 1.3 ± 0.7 | 1.5 ± 0.8 | 1.5 ± 0.8 |
| | $(1.8^{+1.0}_{-0.4}$ | $2.1^{+1.2}_{-0.5}$ | $2.2^{+1.3}_{-0.6})^b$ |
| J1326−0005 | 2.9 ± 1.7 | 3.0 ± 1.7 | 6.0±3.1 |
| | 5.6 ± 1.3 | 5.7 ± 1.3 | 11.4 ± 2.6 |
| J1549+1245 | $0.3^{+0.6}_{-0.1}$ | $0.15^{+0.30}_{-0.08}$ | $0.2^{+0.4}_{-0.1}$ |
| | 6.8 ± 1.2 | 3.1 ± 0.7 | 4.7 ± 0.9 |

**Notes.** Columns give the following information: (1) SDSS ID; (2) observed [OIII] flux (in units of $10^{-15}$ erg cm$^{-2}$ s$^{-1}$); (3) observed [OIII] luminosity; and (4) intrinsic [OIII] luminosity (in units of $10^{44}$ erg s$^{-1}$). The latter was calculated using $E(B-V)$ values derived in Sect. 4.2. $^{(a)}$ Values derived for the broad [OIII] component at 5007 Å (see Sect. 5.1). $^{(b)}$ Values derived for the additional broad, shifted [OIII] component included in models C1 and C2 (see Sect. 4.1).

with $L^{Tot}_{[OIII]} \lesssim 10^{43}$ erg s$^{-1}$. Details about these observations will be discussed in a forthcoming paper by Vietri et al.

### 6.2. Mass rate and kinetic power of ionised outflows

In the following, we calculate the mass rate ($\dot{M}$) and kinetic power ($\dot{E}_{kin}$) of the ionised outflows in our WISSH quasars using the [OIII] emission line as ionised gas mass tracer, similar to many previous studies (e.g. Harrison et al. 2012, 2014; Cano-Díaz et al. 2012; Liu et al. 2013; Brusa et al. 2015; Kakkad et al. 2016). However, we are aware that [OIII] is not a robust mass tracer, as it is very sensitive to gas temperature (and, therefore, metallicity), ionisation parameter, and electron density. Nonetheless, for our targets this emission line is the only observed transition not affected by BLR motions and, therefore, the only available tracer to estimate (at least roughly) the ionised outflowing gas properties.

We assume a spherically/biconically symmetric mass-conserving free wind with a mass outflow rate and velocity that are independent of radius as in Rupke et al. (2002, 2005). We derive the outflowing ionised gas mass from the luminosity associated with the broad [OIII] emission, under the strong assumption that most of the oxygen consists of $O^{2+}$ ions, using the following relation from Carniani et al. (2015):

$$M^{out}_{ion} = 4.0 \times 10^7\, M_\odot \left(\frac{C}{10^{[O/H]}}\right)\left(\frac{L_{[OIII]}}{10^{44}\ \mathrm{erg\,s^{-1}}}\right)\left(\frac{\langle n_e\rangle}{10^3\ \mathrm{cm^{-3}}}\right)^{-1}, \quad (2)$$

where $C = \langle n_e\rangle^2/\langle n_e^2\rangle$ and $n_e$ is the electron density. According to this simple model, in which an ionised cloud uniformly filled up

**Table 6.** Properties of the outflows discovered in the five WISSH quasars.

| SDSS | | $\Delta v^a$ | $v_{\rm max}{}^b$ | $M^{\rm out}_{\rm ion}$ | $\dot{M}$ | $\dot{E}_{\rm kin}$ | $\dot{E}_{\rm kin}/L_{\rm Bol}$ |
|---|---|---|---|---|---|---|---|
| (1) | | (2) | (3) | (4) | (5) | (6) | (7) |
| J0745+4734 | | $-510 \pm 150$ | $1890 \pm 170$ | 6.9 | 5700 | 6.7 | 0.007 |
| J0900+4215 | | $-480 \pm 160$ | $2380 \pm 180$ | 3.2 | 3300 | 6.3 | 0.008 |
| J1201+1206 | (I)$^c$ | – | $1420 \pm 160$ | 3.1 | 2500 | 2.8 | 0.005 |
| | (II)$^c$ | $-1060 \pm 120$ | $1850 \pm 180$ | 0.9 | 740 | 0.9 | 0.001 |
| | (III)$^c$ | $-1990 \pm 200$ | $3270 \pm 230$ | 1.3 | 1890 | 6.7 | 0.012 |
| J1326−0005 | | $-580 \pm 100$ | $2160 \pm 170$ | 8.2 | 7740 | 12.0 | 0.031 |
| J1549+1245 | | $+330 \pm 130$ | $1380 \pm 220$ | 2.9 | 1740 | 1.1 | 0.002 |

**Notes.** Columns give the following information: (1) SDSS ID; (2) velocity shift (in units of km s$^{-1}$); (3) maximum outflow velocity (in units of km s$^{-1}$); (4) ionised outflowing gas mass (in units of $10^9$ $M_\odot$); (5) mass outflow rate (in units of $M_\odot$ yr$^{-1}$); (6) kinetic power (in units of $10^{45}$ erg s$^{-1}$) of the outflow; and (7) ratio between the kinetic power of the outflow and the bolometric luminosity of the quasar. See Sect. 6.2 for a detailed description of the assumptions made to derive $M^{\rm out}_{\rm ion}$, $\dot{M}$, and $\dot{E}_{\rm kin}$. $^{(a)}$ The velocity shift $\Delta v$ of the broad [OIII] component was derived from the shift in wavelength (− sign indicates a blueshift, + sign indicates a redshift) between broad/shifted and narrow/systemic [OIII] centroids. $^{(b)}$ The outflow maximum velocity has been computed as $v_{\rm max} = |\Delta v| + 2\sigma^{\rm broad}_{\rm [OIII]}$. $^{(c)}$ Values derived (I) for the broad component centred at 5007 Å (see Sect. 5.1); (II) for the broad blueshifted component centred at $\lambda \sim 4990$ Å; (III) for the additional broad blueshifted component centred at $\lambda \sim 4970$ Å.

to a certain radius $R$ is ejected outwards of the central regions in the quasar host galaxy, and considering that the mass outflow rate is equal to the total ionised gas mass divided by the dynamical timescale (the time necessary for the mass $M^{\rm out}_{\rm ion}$ to pass through the sphere of radius $R$), we obtain

$$\dot{M} \approx \frac{M^{\rm out}_{\rm ion} v}{R}, \tag{3}$$

where $v$ is the outflow velocity. Therefore:

$$\dot{M} \approx 41\ M_\odot\ {\rm yr}^{-1} \left(\frac{C}{10^{[O/H]}}\right)\left(\frac{L_{[OIII]}}{10^{44}\ {\rm erg\ s^{-1}}}\right)\left(\frac{\langle n_{\rm e}\rangle}{10^3\ {\rm cm^{-3}}}\right)^{-1}\left(\frac{v}{10^3\ {\rm km\ s^{-1}}}\right)\left(\frac{R}{1\ {\rm kpc}}\right)^{-1} \tag{4}$$

Another estimate of $\dot{M}$ is provided by the fluid field continuity equation: if $\rho = \frac{3M^{\rm out}_{\rm ion}}{\Omega\pi R^3}$ is the mean density of an outflow covering the solid angle $\Omega\pi$, then the $\dot{M}$ is given by

$$\dot{M} = \Omega\pi R^2 \rho v = 3\frac{M^{\rm out}_{\rm ion} v}{R}, \tag{5}$$

i.e. a factor of 3 larger than the value derived from Eq. (4). This is a local estimate of $\dot{M}$ at a given radius $R$ (e.g. Feruglio et al. 2015). From $\dot{M}$, the kinetic power associated with the outflow can be derived as follows:

$$\dot{E}_{\rm kin} = \frac{1}{2}\dot{M}v^2. \tag{6}$$

We compute the $\dot{M}$ and $\dot{E}_{\rm kin}$ for our WISSH quasars according to Eqs. (5) and (6), respectively. More specifically, we assume $C \approx 1$, [O/H] $\sim 0$ (solar metallicity) and an electron density $n_{\rm e} = 200$ cm$^{-3}$, as this represents the average value among the samples presented in Figs. 6 and 7. Typical [SII]-based measures of electron density vary from $n_{\rm e} \sim 100$ (e.g. Perna et al. 2015a) up to $n_{\rm e} \sim 500$ cm$^{-3}$ (Nesvadba et al. 2006). According to our simple model, the maximum velocity $v_{\rm max} = |\Delta v| + 2\sigma^{\rm broad}_{\rm [OIII]}$, where $\Delta v$ is the velocity shift between broad and core [OIII] emission centroids, can be considered as representative of the bulk velocity of the outflowing gas. The $v_{\rm max}$ represents the outflow velocity (assumed constant with radius and spherically symmetric) along the line of sight. In our calculations of outflow parameters, we use $v_{\rm max}$ (e.g. Genzel et al. 2011; Cano-Díaz et al. 2012; Brusa et al. 2015) and the intrinsic broad [OIII] luminosity values listed in Tables 6 and 5, respectively.

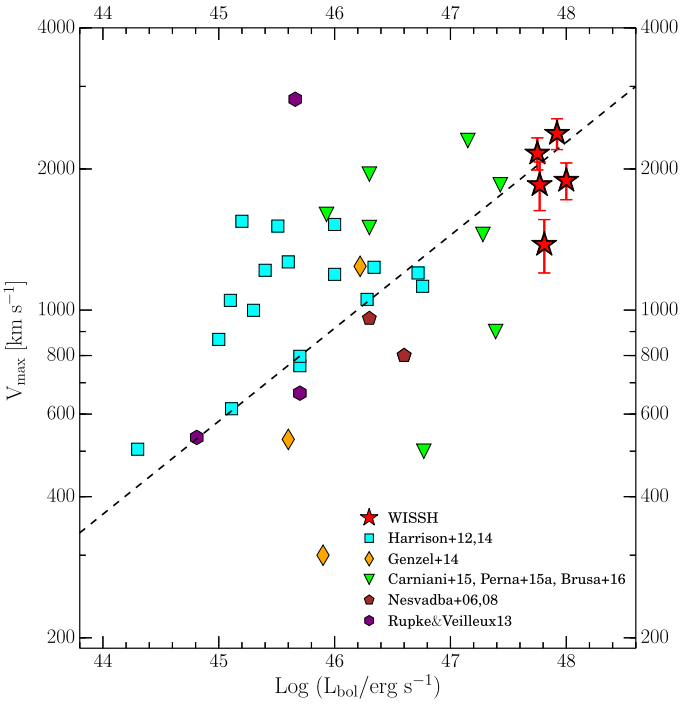


**Fig. 6.** Maximum velocity of the outflow versus the AGN $L_{\rm Bol}$ of the WISSH quasars compared with other samples from literature (i.e. Harrison et al. 2012, 2014; Genzel et al. 2014; Carniani et al. 2015; Perna et al. 2015a; Brusa et al. 2016; Nesvadba et al. 2006, 2008; Rupke & Veilleux 2013). The dashed line represents the relation $L_{\rm Bol} \propto v^5_{\rm max}$ (with arbitrary normalisation) expected for energy conserving winds (see Costa et al. 2014).

The values provided here represent a rough estimate of the $\dot{M}$ and $\dot{E}_{\rm kin}$ of the ionised wind since Eq. (2) is based on several assumptions that lead to an uncertainty level on $\dot{M}$ up to an order of magnitude. A comprehensive description of these assumptions and their impact on the determination of the outflow

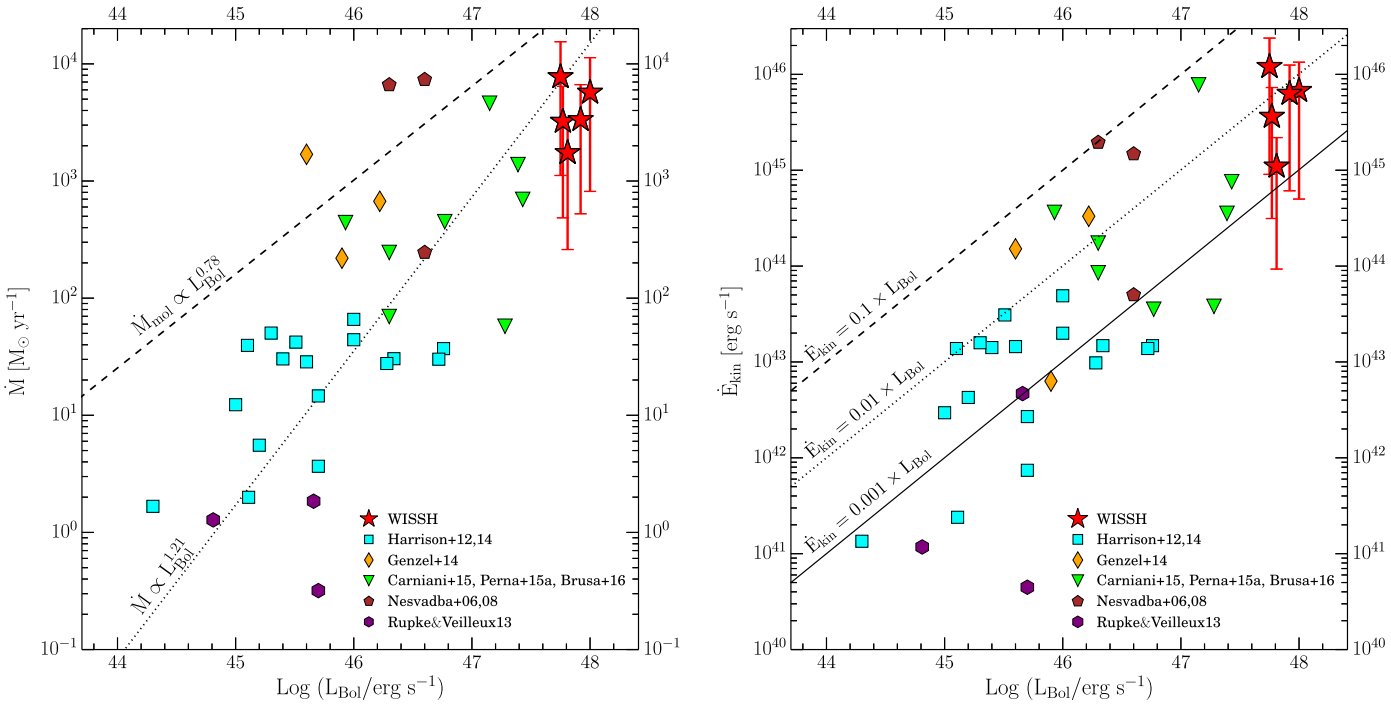


(a) (b)

**Fig. 7.** Mass rate **a)** and kinetic power **b)** of the ionised outflows as a function of $L_{Bol}$. Values obtained for the WISSH quasars (red stars) are compared with other samples from literature (i.e. Harrison et al. 2012, 2014; Genzel et al. 2014; Carniani et al. 2015; Perna et al. 2015a; Brusa et al. 2016; Nesvadba et al. 2006, 2008; Rupke & Veilleux 2013). Error bars are calculated as described in Sect. 6.2. In panel **a)** the dotted line corresponds to the best-fit relation $\dot{M} \propto L_{Bol}^{1.21}$ derived for ionised outflows and the dashed line indicates the $\dot{M} \propto L_{Bol}^{0.78}$ best-fit relation to molecular outflows (see Fiore et al. 2016, for a complete discussion). In panel **b)** dashed, dotted, and solid lines represent an outflow kinetic power that is 10%, 1%, and 0.1% of the AGN luminosity, respectively.

parameters is presented in Kakkad et al. (2016), which provides further details.

Furthermore, because of the lack of accurate information on the spatial scale of the outflowing gas, we assume $R \sim 7$ kpc as the radius of the emitting broad [OIII] region. We consider this a reasonable assumption based on the results presented in Sect. 5.2, as it corresponds to the spatial scale at which we observe fast extended [OIII] in J1201+1206 and J1326−0005. We stress that this choice implies conservative values of $\dot{M}$ and $\dot{E}_{kin}$, as it maximises the spatial scale of the outflows. Smaller values of the radius would lead to even higher values (see Eq. (5)).

Figures 6, 7a, and 7b show the values derived for our WISSH quasars of $v_{max}$, $\dot{M}$ and $\dot{E}_{kin}$ as a function of $L_{Bol}$, respectively. In case of J1201+1206, we plot the $v_{max}$, $\dot{M}$ and $\dot{E}_{kin}$ obtained from the best fit without considering the additional broad, blueshifted OIII component included in model C1 (see Sect. 4). Including the additional component would lead to larger $\dot{M}$ and $\dot{E}_{kin}$ (see Table 6). We compare our findings with those of (i) obscured X-ray selected quasars studied by Brusa et al. (2016) and Perna et al. (2015a); (ii) [OIII]-loud, hyper-luminous ($L_{Bol} > 10^{47}$ erg s$^{-1}$) quasars at $z \sim 1.5$−2.5 in Carniani et al. (2015); (iii) high-$z$ radio-galaxies analysed by Nesvadba et al. (2006, 2008); (iv) low-$z$ and high-$z$ (mostly Type 2) AGN with [OIII] outflows from Harrison et al. (2012, 2014); and (v) massive AGN at $z \sim 2$ from Genzel et al. (2014).

Figure 6 suggests a correlation between maximum outflow velocity and AGN luminosity, with all the ionised outflows discovered in WISSH quasars exhibiting among the largest $v_{max}$ values ($\gtrsim$1300 km s$^{-1}$). As previously reported by Shen (2016), Zakamska & Greene (2014), and Zakamska et al. (2016), the [OIII] emission lines detected in luminous AGN tend to have larger widths. Interestingly, the observed values are consistent with a $L_{Bol} \propto v_{max}^5$ relation, which is expected for an energy conserving wind (Costa et al. 2014).

Some samples included in Fig. 7 have published $\dot{M}$ values derived from the luminosity of H$\alpha$ or H$\beta$ instead of [OIII] luminosity. This leads to values of $\dot{M}$ that are systematically larger by a factor of ∼3 up to 10 than those computed from the [OIII] (Fiore et al. 2016). This discrepancy can be due to the fact that Balmer and [OIII] lines are produced in regions with different C and $n_e$ values and to the assumption that $n(O^{2+})/n(O) \sim 1$ in the derivation of Eq. (2) (Carniani et al. 2015). Accordingly, to enable a proper comparison, all the [OIII]-based ionised gas masses (and, hence, $\dot{M}$ and $\dot{E}_{kin}$) were multiplied by a conservative factor of 3 (including those of our WISSH quasars). The alternative estimate of the mass outflow rate from the broad H$\beta$ in our WISSH quasars is a factor of ∼3.2 larger than the $\dot{M}$ derived from the [OIII] emission. Furthermore, to compare homogeneous values, all $\dot{M}$ and $\dot{E}_{kin}$ shown in Figs. 7a,b have been inferred using the same assumptions adopted for WISSH quasars, (i.e. $n_e = 200$ cm$^{-3}$ and $v_{max}$). Our objects exhibit huge values of $\dot{M}$, i.e. from $\sim 1.7 \times 10^3$ up to $\sim 7.7 \times 10^3$ $M_\odot$ yr$^{-1}$, and $\dot{E}_{kin} \sim 10^{45}$−$10^{46}$ erg s$^{-1}$(see Table 6), which are among the largest values measured so far.

In order to give an idea of the potential impact of the uncertainties affecting $\dot{M}$ and $\dot{E}_{kin}$, we report error bars for WISSH

quasars in Fig. 7 estimated as follows: the upper bounds correspond to the assumption of $n_e = 80$ cm$^{-3}$ (as in Genzel et al. 2014), while the lower bounds correspond to $n_e = 1000$ cm$^{-3}$ (i.e. the typical value for the NLR, Peterson 1997) and a velocity of $W_{80}/1.3$ (as in Harrison et al. 2014), with $W_{80}$ the velocity width of the line at the 80% of the line flux. For our sources, $W_{80}$ is a factor of 1.3–1.8 smaller than $v_{max}$. However, we stress that these estimates of the outflow parameters are based on a very simplistic scenario because of the limited information on the physical properties of the [OIII] emitting material.

Both $\dot{M}$ and $\dot{E}_{kin}$ seem to exhibit a correlation with $L_{Bol}$, although with a large scatter. We note that WISSH quasars show less scatter than other samples in Fig. 7. The increase of mass outflow rates with increasing $L_{Bol}$ is consistent with a theoretical scenario according to which the more luminous the AGN, the more the amount of gas is invested by a radiatively driven wind (Menci et al. 2008). However, a direct relation between $v_{max}$ and $L_{Bol}$ is difficult to be established via observations, as the fraction of the outflow kinetic power injected into the ISM may be different from object to object. Moreover, the $L_{Bol}$ derived here may not represent the long timescale average luminosity of the AGN, which is responsible for the outflow acceleration (Faucher-Giguère & Quataert 2012). All these effects can produce the observed large scatter.

Figure 7a suggests that ionised outflows, revealed at the highest luminosities, may trace a larger fraction of the total outflowing gas than outflows in low luminosity AGN. The best-fit relation $\dot{M} \propto L_{Bol}^{1.21}$ for the ionised outflows is steeper than the relation $\dot{M}_{mol} \propto L_{Bol}^{0.78}$ obtained for molecular outflows (see Fiore et al. 2016, for a complete discussion), indicating that at $L_{Bol} \gtrsim 10^{47}$ the mass rates of ionised and molecular outflows become comparable. This is also supported by the fact that most of $\dot{E}_{kin}$ values derived for our WISSH quasars are broadly consistent with a fraction of ∼1% of $L_{Bol}$ and, remarkably, in case of J1326−0005, the ratio $\dot{E}_{kin}/L_{Bol}$ reaches a value of ∼3%. These values are therefore very close to the predictions (i.e. $\dot{E}_{kin}/L_{Bol} \sim 5\%$) of the vast majority of AGN feedback models (e.g. Di Matteo et al. 2005; Zubovas & King 2012) for an efficient feedback mechanism to be able to account for the $M_{BH}$–$\sigma$ relation. Similar fractions have been indeed observed for molecular outflows (Feruglio et al. 2010; Cicone et al. 2014), whereas ionised outflows usually show values <1% of $L_{Bol}$ as illustrated in Fig. 7b.

Finally, we note that assuming a density profile $n_e \propto r^{-2}$ (where $r$ is the distance from the galaxy centre) as for an isothermal scenario, leads to mass outflow rates reduced by a factor of ∼3 with respect to the values derived considering a uniform density. However, all $\dot{M}$ and $\dot{E}_{kin}$ plotted in Fig. 7 should be reduced by a similar factor, and the positive trend with increasing $L_{Bol}$ therefore remains valid.

## 7. Summary and conclusions

In this work, we analysed the LBT/LUCI1 optical rest-frame spectra of five broad-line quasars at $z \sim 2.5$–$3.5$ with the aim of characterising nuclear properties and AGN-driven outflows at the brightest end of the AGN luminosity function. Our targets belong to the WISE/SDSS selected hyper-luminous (WISSH) quasars sample and all have $L_{Bol} \gtrsim 6 \times 10^{47}$ erg s$^{-1}$. We traced the ionised gas kinematics from the broad wings of the [OIII] emission line and estimated the mass of the SMBH from the BLR H$\beta$ emission. Our key findings can be summarised as follows:

- Our spectral analysis reveals the presence of very broad (FWHM$^{broad}_{[OIII]} \sim 1200$–$2200$ km s$^{-1}$) [OIII] emission lines (among the largest measured so far), with exceptional luminosities $L^{Tot}_{[OIII]} \gtrsim 5 \times 10^{44}$ erg s$^{-1}$ (see Fig. 5). This finding suggests that our WISE/SDSS selection allows us to extend the study of ionised outflows up to $L^{broad}_{[OIII]} \gtrsim 10^{45}$ erg s$^{-1}$. We also find that the WISSH quasars with the largest [OIII] luminosity (>$10^{45}$ erg s$^{-1}$) typically show a small ratio (∼2–7) between the luminosity of the broad and narrow, systemic [OIII] component.
- The "off-nuclear" spectra of three out of five quasars, extracted at increasing distances from the central source, show hints of extended [OIII] emission on scale of ∼7–10 kpc, associated with outflowing gas in J1201+1206 and J1326−0005 (see Sect. 5.2). Furthermore, we are able to reveal a likely bipolar outflow in J1201+1206, with a redshifted (blueshifted) [OIII] component seen north (south) off the nucleus out to ∼7 kpc.
- Our WISSH quasars host SMBHs with very large H$\beta$-based masses ($M^{H\beta}_{BH} \gtrsim 2 \times 10^9$ $M_\odot$), which are accreting at high rates ($\lambda_{Edd}$ from ∼0.4 up to 3). This suggests that WISSH quasars are highly accreting SMBHs at the massive end of the SMBH mass function (see Sect. 5.3).
- We find ionised outflows exhibiting huge values of $\dot{M} \sim 1700$–$7700$ $M_\odot$ yr$^{-1}$ and $\dot{E}_{kin} \sim 10^{45}$–$10^{46}$ erg s$^{-1}$, indicating that WISSH quasars allow us to reveal extreme outflows. We derive $\dot{M}$ values that are closer to the best-fit $\dot{M}_{mol}$–$L_{Bol}$ relation, derived for galaxy-wide molecular outflows in Fiore et al. (2016), than values typically observed in lower AGN luminosity (see Fig. 7). This finding, in addition to the large $\dot{E}_{kin}/L_{Bol} \sim 0.01$–$0.03$, suggests that the ionised outflows in hyper-luminous quasars may trace a substantial fraction of the outflowing gas. However, one should bear in mind that our estimates of $\dot{M}$ and $\dot{E}_{kin}$ are affected by order-of-magnitude uncertainties because of the use of [OIII] as tracer of the ionised outflows and the very basic outflow model we assumed (see Sect. 6.2 and Kakkad et al. 2016).

This paper presents the first results about the presence of powerful ionised winds in WISSH quasars. A complete description of the optical rest-frame spectral properties for a larger sample of WISSH quasars covered by LUCI1 observations will be provided in a forthcoming paper (Vietri et al.). Furthermore, a follow-up programme of J1326−0005 and J1201+1206 with the VLT SINFONI integral field spectrograph (P.I. Bongiorno) has been recently accepted. These observations will enable us to accurately constrain the morphology and, in turn, the effects on the host galaxy ISM of these energetic outflows.

*Acknowledgements.* We are grateful to the anonymous referee for valuable feedback that helped to improve the paper. Based on observations obtained at the LBT. The LBT is an international collaboration among institutions in the United States, Italy, and Germany. LBT Corporation partners are: The University of Arizona on behalf of the Arizona Board of Regents; Istituto Nazionale di Astrofisica, Italy; LBT Beteiligungsgesellschaft, Germany, representing the Max-Planck Society, the Astrophysical Institute Potsdam, and Heidelberg University; The Ohio State University, and The Research Corporation, on behalf of The University of Notre Dame, University of Minnesota and University of Virginia. This research has made use of the NASA/IPAC Extragalactic Database (NED), which is operated by the Jet Propulsion Laboratory, California Institute of Technology, under contract with the National Aeronautics and Space Administration. We acknowledge financial support from PRIN-INAF 2014. A. Bongiorno and E. Piconcelli acknowledge financial support from INAF under the contract PRIN-INAF-2012. M. Brusa acknowledges support from the FP7 Career Integration Grant "eEasy"

(CIG 321913). R. Schneider and M. Bischetti acknowledge funding from the ERC FP7 (Grant Agreement No. 306476). L. Zappacosta acknowledges financial support2D under ASI/INAF contract I/037/12/0. We thank E. Lusso and S. Carniani for providing us with $L_{\rm Bol}$ and $M_{\rm BH}$ values for the COSMOS sources, and the $\rm FWMH_{OIII}$ and $L_{\rm OIII}$ values plotted in Figs. 4 and 5, respectively. We also thank S. Gallerani for kindly providing the extinction curve from Gallerani et al. (2010) in digital form. We are grateful to M. Fumana for the assistance in data reduction and M. Perna for useful discussion on off-nuclear spectra.

## References

Ahn, C. P., Alexandroff, R., Allende Prieto, C., et al. 2014, ApJS, 211, 17
Baskin, A., & Laor, A. 2005, MNRAS, 356, 1029
Bongiorno, A., Maiolino, R., Brusa, M., et al. 2014, MNRAS, 443, 2077
Boroson, T. A., & Green, R. F. 1992, ApJS, 80, 109
Bouché, N., Cresci, G., Davies, R., et al. 2007, ApJ, 671, 303
Brusa, M., Bongiorno, A., Cresci, G., et al. 2015, MNRAS, 446, 2394
Brusa, M., Perna, M., Cresci, G., et al. 2016, A&A, 588, A58
Bruzual, G., & Charlot, S. 2003, MNRAS, 344, 1000
Calzetti, D., Armus, L., Bohlin, R. C., et al. 2000, ApJ, 533, 682
Cano-Díaz, M., Maiolino, R., Marconi, A., et al. 2012, A&A, 537, L8
Carniani, S., Marconi, A., Maiolino, R., et al. 2015, A&A, 580, A102
Carniani, S., Marconi, A., Maiolino, R., et al. 2016, A&A, 591, A28
Cicone, C., Maiolino, R., Sturm, E., et al. 2014, A&A, 562, A21
Costa, T., Sijacki, D., & Haehnelt, M. G. 2014, MNRAS, 444, 2355
Cresci, G., Mainieri, V., Brusa, M., et al. 2015, ApJ, 799, 82
Di Matteo, T., Springel, V., & Hernquist, L. 2005, Nature, 433, 604
Fabian, A. C. 2012, ARA&A, 50, 455
Faucher-Giguère, C.-A., & Quataert, E. 2012, MNRAS, 425, 605
Ferland, G. J., Porter, R. L., van Hoof, P. A. M., et al. 2013, Rev. Mex. Astron. Astrofis., 49, 137
Feruglio, C., Maiolino, R., Piconcelli, E., et al. 2010, A&A, 518, L155
Feruglio, C., Fiore, F., Carniani, S., et al. 2015, A&A, 583, A99
Fiore, F., Feruglio, C., Shankar, F., et al. 2016, A&A, submitted
Gallerani, S., Maiolino, R., Juarez, Y., et al. 2010, A&A, 523, A85
Genzel, R., Newman, S., Jones, T., et al. 2011, ApJ, 733, 101
Genzel, R., Förster Schreiber, N. M., Rosario, D., et al. 2014, ApJ, 796, 7
Gibson, R. R., Jiang, L., Brandt, W. N., et al. 2009, ApJ, 692, 758
Greene, J. E., Zakamska, N. L., Liu, X., Barth, A. J., & Ho, L. C. 2009, ApJ, 702, 441
Harrison, C. M., Alexander, D. M., Swinbank, A. M., et al. 2012, MNRAS, 426, 1073
Harrison, C. M., Alexander, D. M., Mullaney, J. R., & Swinbank, A. M. 2014, MNRAS, 441, 3306
Harrison, C. M., Alexander, D. M., Mullaney, J. R., et al. 2016, MNRAS, 456, 1195
Hopkins, P. F., Strauss, M. A., Hall, P. B., et al. 2004, AJ, 128, 1112
Hopkins, P. F., Hernquist, L., Cox, T. J., & Kereš, D. 2008, ApJS, 175, 356
Hopkins, P. F., Torrey, P., Faucher-Giguère, C.-A., Quataert, E., & Murray, N. 2016, MNRAS, 458, 816
Kakkad, D., Mainieri, V., Padovani, P., et al. 2016, A&A, 592, A148
Kelly, B. C., & Merloni, A. 2012, Adv. Astron., 2012, 970858
Kim, M., Ho, L. C., Lonsdale, C. J., et al. 2013, ApJ, 768, L9
King, A., & Pounds, K. 2015, ARA&A, 53, 115
Liu, G., Zakamska, N. L., Greene, J. E., Nesvadba, N. P. H., & Liu, X. 2013, MNRAS, 436, 2576
Lusso, E., Comastri, A., Simmons, B. D., et al. 2012, MNRAS, 425, 623
Maiolino, R., Gallerani, S., Neri, R., et al. 2012, MNRAS, 425, L66
Markwardt, C. B. 2009, in Astronomical Data Analysis Software and Systems XVIII, eds. D. A. Bohlender, D. Durand, & P. Dowler, ASP Conf. Ser., 411, 251
Menci, N., Fiore, F., Puccetti, S., & Cavaliere, A. 2008, ApJ, 686, 219
Morganti, R., Veilleux, S., Oosterloo, T., Teng, S. H., & Rupke, D. 2016, A&A, 593, A30
Mullaney, J. R., Alexander, D. M., Fine, S., et al. 2013, MNRAS, 433, 622
Nagao, T., Marconi, A., & Maiolino, R. 2006, A&A, 447, 157
Nesvadba, N. P. H., Lehnert, M. D., Eisenhauer, F., et al. 2006, ApJ, 650, 693
Nesvadba, N. P. H., Lehnert, M. D., De Breuck, C., Gilbert, A. M., & van Breugel, W. 2008, A&A, 491, 407
Perna, M., Brusa, M., Cresci, G., et al. 2015a, A&A, 574, A82
Perna, M., Brusa, M., Salvato, M., et al. 2015b, A&A, 583, A72
Peterson, B. M. 1997, An Introduction to Active Galactic Nuclei (Cambridge, New York: Cambridge University Press)
Prevot, M. L., Lequeux, J., Prevot, L., Maurice, E., & Rocca-Volmerange, B. 1984, A&A, 132, 389
Richards, G. T., Hall, P. B., Vanden Berk, D. E., et al. 2003, AJ, 126, 1131
Richards, G. T., Lacy, M., Storrie-Lombardi, L. J., et al. 2006, ApJS, 166, 470
Rieke, G. H., & Lebofsky, M. J. 1985, ApJ, 288, 618
Rodríguez Zaurín, J., Tadhunter, C. N., Rose, M., & Holt, J. 2013, MNRAS, 432, 138
Rupke, D. S. N., & Veilleux, S. 2013, ApJ, 768, 75
Rupke, D. S. N., & Veilleux, S. 2015, ApJ, 801, 126
Rupke, D. S., Veilleux, S., & Sanders, D. B. 2002, ApJ, 570, 588
Rupke, D. S., Veilleux, S., & Sanders, D. B. 2005, ApJS, 160, 115
Shemmer, O., Netzer, H., Maiolino, R., et al. 2004, ApJ, 614, 547
Shen, Y. 2016, ApJ, 817, 55
Shen, Y., & Ho, L. C. 2014, Nature, 513, 210
Shen, Y., & Liu, X. 2012, ApJ, 753, 125
Silk, J., & Rees, M. J. 1998, A&A, 331, L1
Skrutskie, M. F., Cutri, R. M., Stiening, R., et al. 2006, AJ, 131, 1163
Somerville, R. S., Hopkins, P. F., Cox, T. J., Robertson, B. E., & Hernquist, L. 2008, MNRAS, 391, 481
Spoon, H. W. W., Farrah, D., Lebouteiller, V., et al. 2013, ApJ, 775, 127
Tsuzuki, Y., Kawara, K., Yoshii, Y., et al. 2006, ApJ, 650, 57
Urrutia, T., Lacy, M., Spoon, H., et al. 2012, ApJ, 757, 125
Vacca, W. D., Cushing, M. C., & Rayner, J. T. 2003, PASP, 115, 389
Vanden Berk, D. E., Richards, G. T., Bauer, A., et al. 2001, AJ, 122, 549
Véron-Cetty, M.-P., Joly, M., & Véron, P. 2004, A&A, 417, 515
Villar-Martín, M., Humphrey, A., Delgado, R. G., Colina, L., & Arribas, S. 2011, MNRAS, 418, 2032
Weedman, D., Sargsyan, L., Lebouteiller, V., Houck, J., & Barry, D. 2012, ApJ, 761, 184
Wright, E. L., Eisenhardt, P. R. M., Mainzer, A. K., et al. 2010, AJ, 140, 1868
Wyithe, J. S. B., & Loeb, A. 2003, ApJ, 595, 614
Wylezalek, D., & Zakamska, N. L. 2016, MNRAS, 461, 3724
Zakamska, N. L., & Greene, J. E. 2014, MNRAS, 442, 784
Zakamska, N. L., Hamann, F., Pâris, I., et al. 2016, MNRAS, 459, 3144
Zhang, K., Dong, X.-B., Wang, T.-G., & Gaskell, C. M. 2011, ApJ, 737, 71
Zubovas, K., & King, A. 2012, ApJ, 745, L34

## Appendix A: Additional figures

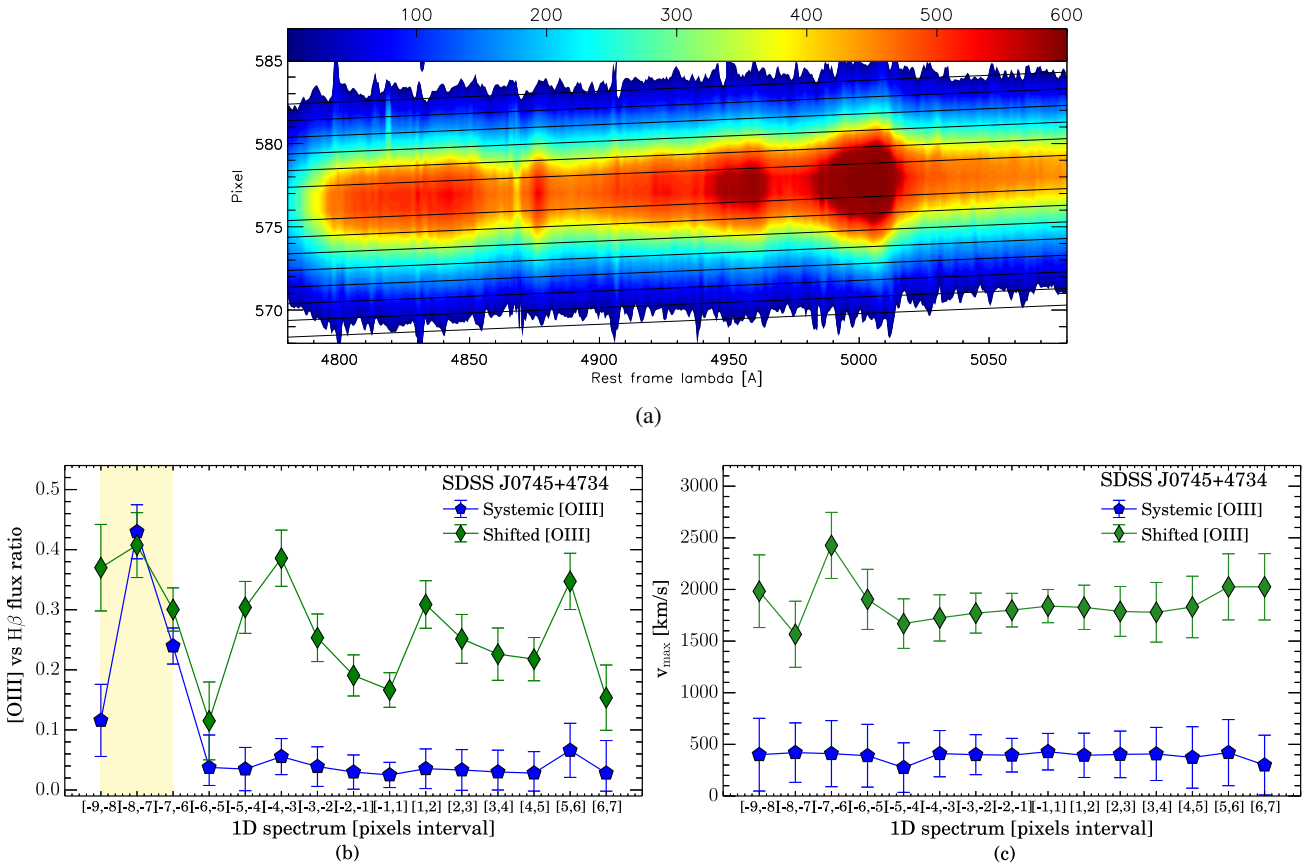


**Fig. A.1.** **a)** 2D LUCI1 spectrum of J0745+4734. Blue to red colours indicate increasing counts. *Top and bottom* correspond to north and south direction, respectively. The black solid lines indicate the apertures used for extracting the off-nuclear spectra. **b)** The integrated flux ratio of the shifted and systemic [OIII] components with respect to the BLR H$\beta$ emission line detected in the "off-nuclear" spectra of J0745+4734 extracted from different apertures. Negative (positive) pixel values correspond to south (north) direction (1 pixel ~ 1.9 kpc at the redshift of J0745+4734). The yellow band highlights the presence of extended [OIII] emission. **c)** Maximum velocity of the shifted and systemic [OIII] components detected in the "off-nuclear" spectra of J0745+4734.

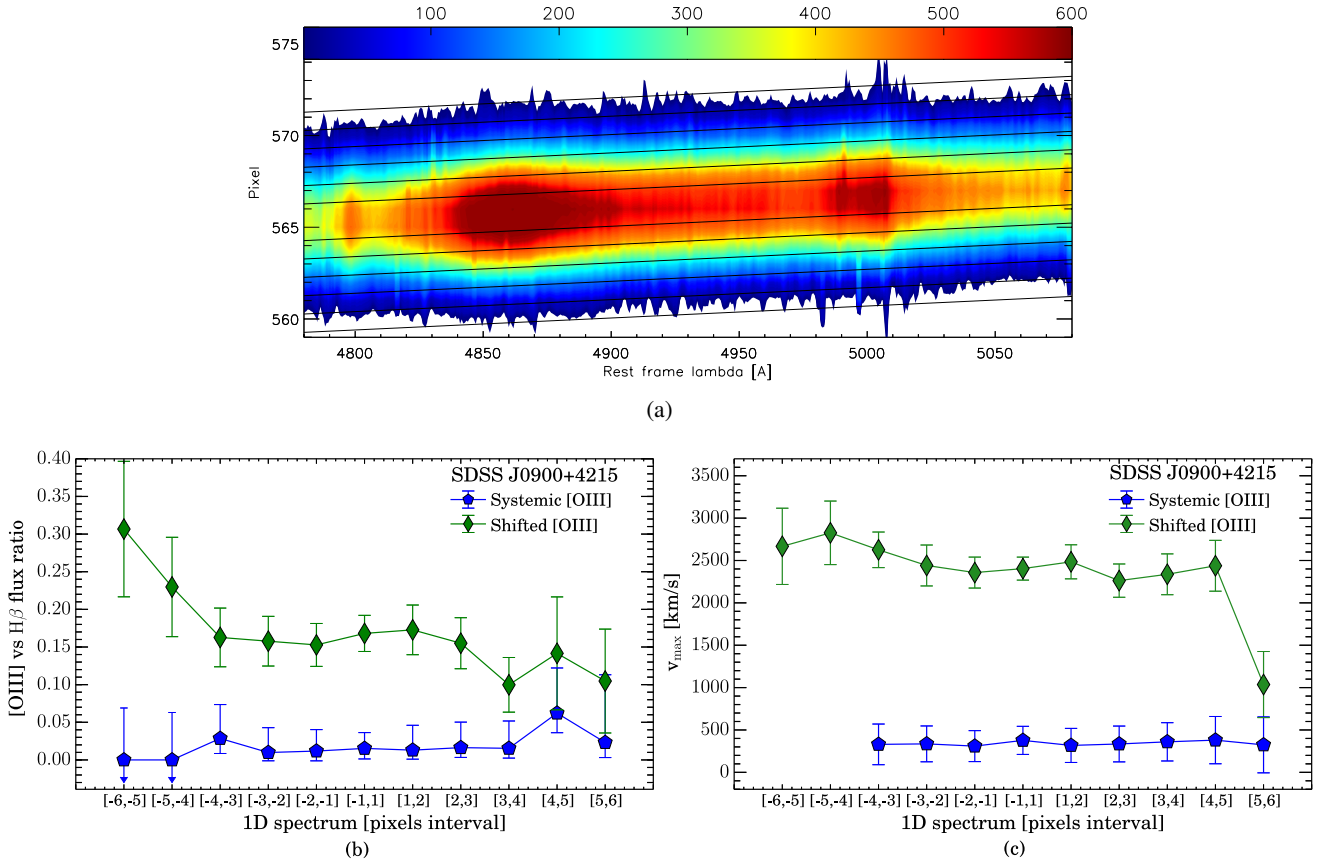


**Fig. A.2.** Same as Fig. A.1 but for J0900+4215 (1 pixel ~ 1.9 kpc at the redshift of this source).

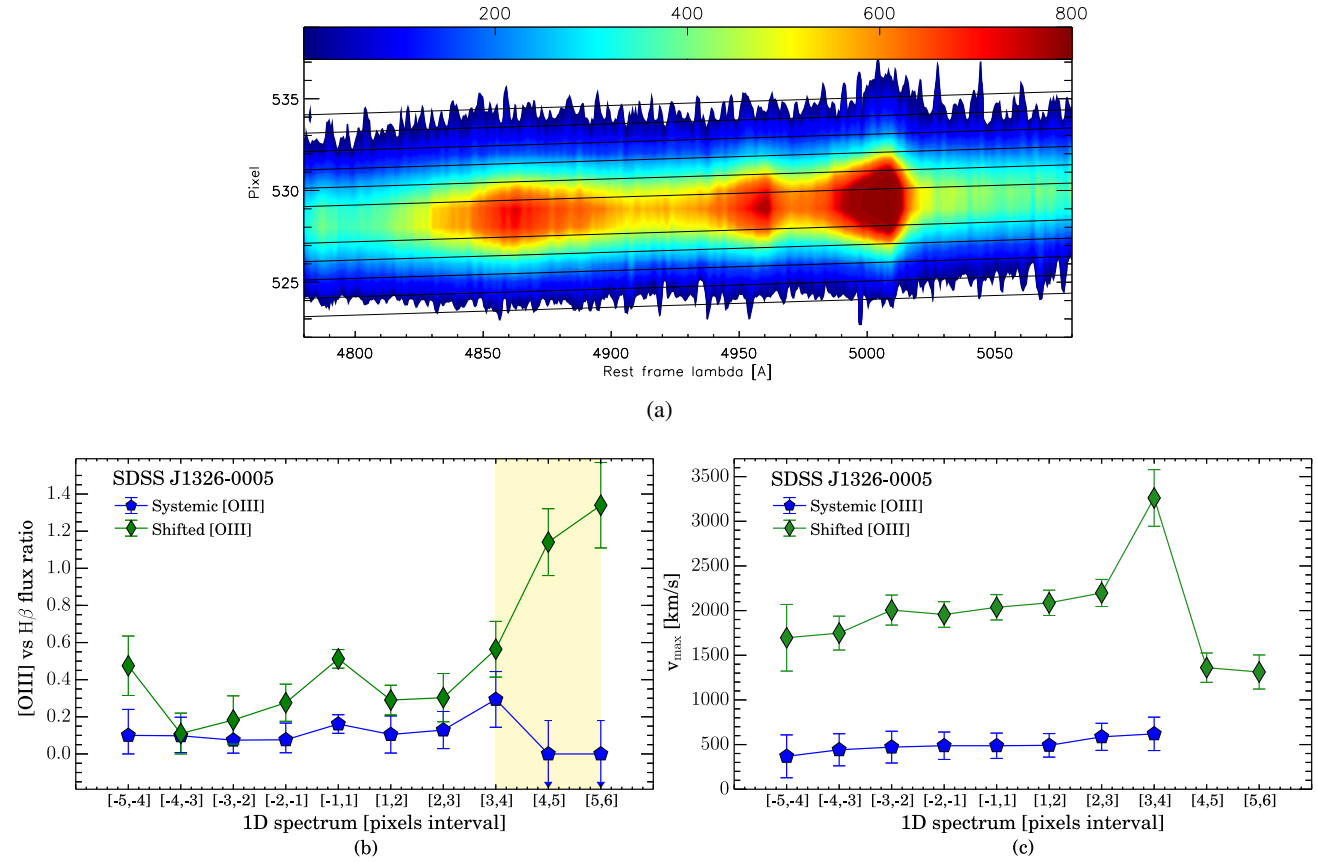


**Fig. A.3.** Same as Fig. A.1 but for J1326−0005 (1 pixel ~ 1.9 kpc at the redshift of this source).

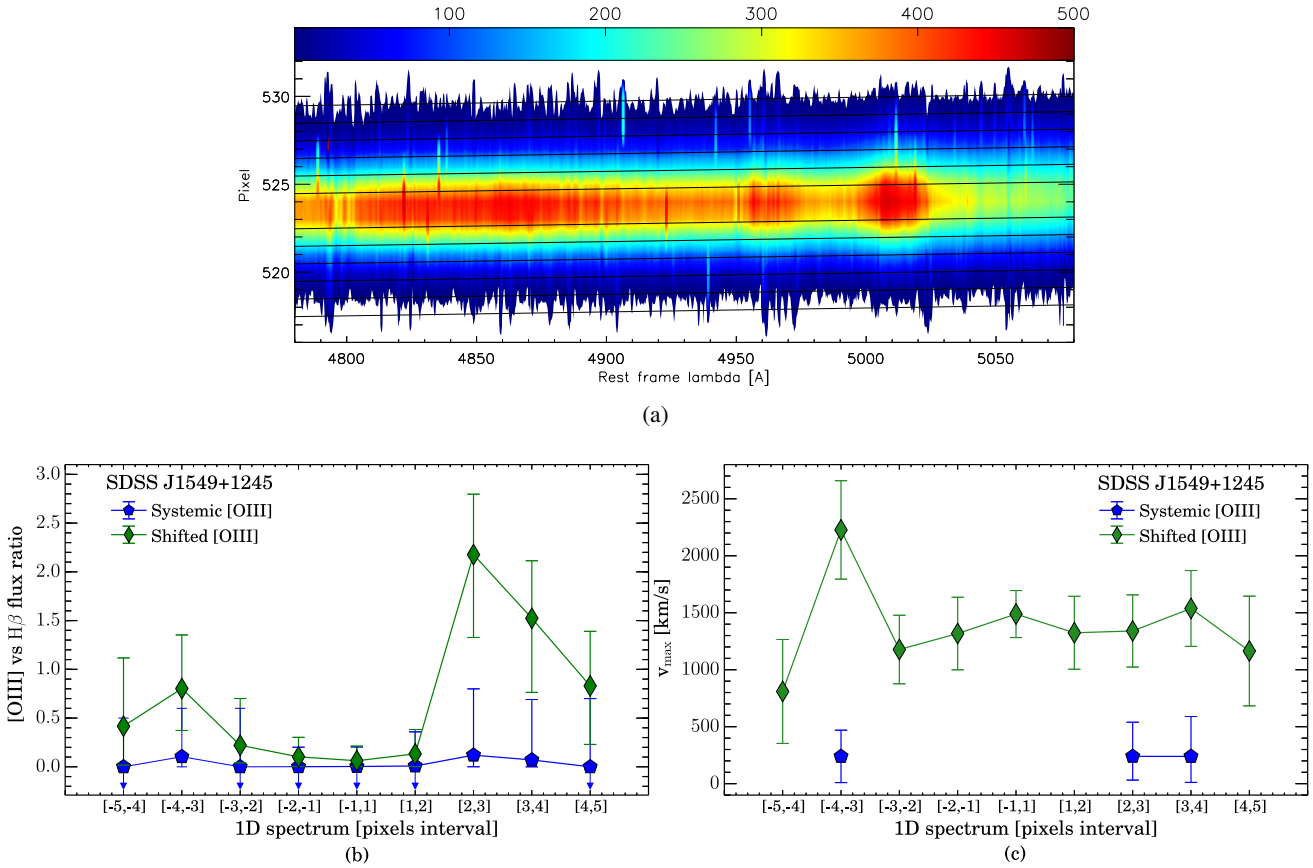


**Fig. A.4.** Same as Fig. A.1 but for J1549+1245 (1 pixel ~ 2.1 kpc at the redshift of this source).